样式定义: 标题 2

POMINO-GEMS：A Research Product for Tropospheric NO₂ Columns from Geostationary Environment Monitoring Spectrometer

Yuhang Zhang[1], Jintai Lin[1], Jhoon Kim[2], Hanlim Lee[3], Junsung Park[3], Hyunkee Hong[4], Michel Van Roozendael[5], Francois Hendrick[5], Ting Wang[6,7], Pucai Wang[6,7], Qin He[8], Kai Qin[8], Yongjoo Choi[9], Yugo Kanaya[10], Jin Xu[11], Pinhua Xie[7,11], Xin Tian[12], Sanbao Zhang[13], Shanshan Wang[13], Siyang Cheng[14], Xinghong Cheng[14], Jianzhong Ma[14], Thomas Wagner[15], Robert ~~Spurr~~[14]Spurr[16], Lulu ~~Chen~~[15]Chen[17], Hao Kong[1], Mengyao ~~Liu~~[16]Liu[18]

[1]Laboratory for Climate and Ocean-Atmosphere Studies, Department of Atmospheric and Oceanic Sciences, School of Physics, Peking University, Beijing, 100871, China

[2]Department of Atmospheric Sciences, Yonsei University, Seoul, South Korea

[3]Pukyong National University, Busan, South Korea

[4]National Institute of Environmental Research, Incheon, South Korea

[5]~~BIRA-IASB, Belgian~~[5]Belgian Institute for Space Aeronomy~~,~~ (BIRA-IASB), Brussels, Belgium

[6]CNRC & LAGEO, Institute of Atmospheric Physics, Chinese Academy of Sciences, Beijing, 100029, China

[7]University of Chinese Academy of Sciences, Beijing, 100049, China

[8]School of Environment and Geoinformatics, China University of Mining and Technology, Xuzhou, Jiangsu, 221116, China

[9]Department of Environmental Science, Hankuk University of Foreign Studies, Yongin, South Korea

[10]Research Institute for Global Change, Japan Agency for Marine-Earth Science and Technology (JAMSTEC), Yokohama, 2360001, Japan

[11]Key Laboratory of Environmental Optics and Technology, Anhui Institute of Optics and Fine Mechanics, Chinese Academy of Science, Hefei, 230031, China

[12]Information Materials and Intelligent Sensing Laboratory of Anhui Province, Institutes of Physical Science and Information Technology, Anhui University, Hefei, Anhui, 230601, China

[13]Shanghai Key Laboratory of Atmospheric Particle Pollution and Prevention (LAP3), Department of Environmental Science and Engineering, Fudan University, Shanghai, 200433, China

~~[14]RT~~[14]State Key Laboratory of Severe Weather & Institute of Tibetan Plateau Meteorology, Chinese Academy of Meteorological Sciences, Beijing, 100081, China

[15]Max Planck Institute for Chemistry, 55020, Mainz, Germany

[16]RT Solutions Inc., Cambridge, Massachusetts, 02138, USA

~~[15]College~~[17]College of Urban and Environmental Sciences, Peking University, Beijing, 100871, China

~~[16]R~~[18]R&D Satellite Observations Department, Royal Netherlands Meteorological Institute, De Bilt, the Netherlands

Correspondence to: Jintai Lin (linjt@pku.edu.cn)

Abstract

~~Nitrogen dioxide (NO₂) is a major air pollutant.~~ Tropospheric ~~NO₂~~ vertical column densities (VCDs) of nitrogen dioxide (NO₂) retrieved from sun-synchronous satellite instruments have provided abundant

NO$_2$ data for environmental studies, but such data are limited by <u>retrieval uncertainties and</u> insufficient temporal sampling (e.g., once a day). The Geostationary Environment Monitoring Spectrometer (GEMS) launched in February 2020 monitors NO$_2$ at an unprecedented ~~high temporal~~<u>hourly</u> resolution <u>during the daytime</u>. Here we present a research product for tropospheric NO$_2$ VCDs, referred to as POMINO-GEMS. We develop a hybrid retrieval method combining GEMS ~~and~~<u>,</u> TROPOMI ~~observations as well as~~ <u>and</u> GEOS-~~Chem simulations~~<u>CF data</u> to generate hourly tropospheric NO$_2$ slant column densities (SCDs). We then derive tropospheric NO$_2$ air mass factors (AMFs) with explicit corrections for ~~the anisotropy of~~ surface reflectance <u>anisotropy</u> and aerosol optical effects, through <u>parallelized</u> pixel-by-pixel radiative transfer calculations. Prerequisite cloud parameters are retrieved with the O$_2$-O$_2$ algorithm by using ancillary parameters consistent with those used in NO$_2$ AMF calculations.

Initial retrieval of POMINO-GEMS tropospheric NO$_2$ VCDs for June–August 2021 ~~reveals~~<u>exhibits</u> strong hotspot signals over megacities and distinctive diurnal variations over polluted and clean areas. POMINO-GEMS NO$_2$ VCDs agree ~~well~~ with ~~our~~<u>the</u> POMINO-TROPOMI v1.2.2 product (R = 0.~~97~~<u>98</u>, and NMB = ~~3.6~~<u>4.9</u>%) over <u>East</u> Asia. ~~Comparison~~<u>,</u> with <u>slight differences associated with satellite viewing geometries and cloud and aerosol properties affecting the NO$_2$ retrieval. POMINO-GEMS also shows good agreement with OMNO2 v4 (R = 0.87, and NMB = −16.8%) and GOME-2 GDP 4.8 (R = 0.83, and NMB = −1.5%) NO$_2$ products. POMINO-GEMS shows small biases against</u> ground-based MAX-DOAS <u>NO$_2$</u> VCD data at nine sites ~~shows a small bias of POMINO-GEMS~~ (NMB = ~~−15.7%); however, the~~<u>11.1%)</u> <u>with modest or high</u> correlation ~~for~~<u>in</u> diurnal variation ~~varies~~<u>at six urban and suburban sites (R</u> from ~~0.66~~<u>60</u> to 0.~~90, suggesting location-dependent performance.~~<u>96). The spatiotemporal variation of POMINO-GEMS correlates well with mobile-car MAX-DOAS measurements in the Three Rivers' Source region on the Tibetan Plateau (R = 0.81).</u> Surface NO$_2$ concentrations estimated from POMINO-GEMS VCDs are consistent with measurements from the Ministry of Ecology and Environment of China ~~at 855 sites~~ <u>(for spatiotemporal variation (R = 0.78, and</u> NMB = ~~−24.1%, and *R* = 0.95 for~~<u>26.3%) as well as</u> diurnal ~~correlation averaged over~~<u>variation at all,</u> <u>urban, suburban and rural</u> sites <u>($R \geq$ 0.96)</u>. POMINO-GEMS data will be made freely available for users to study the spatiotemporal variations, sources and impacts of NO$_2$.

1. Introduction

Tropospheric nitrogen dioxide (NO$_2$) is an important air pollutant. It ~~is a threat to~~<u>threats</u> human

68 health, and ~~also~~ contributes to the formation of tropospheric ozone (O_3) and nitrate ~~aerosol as an essential~~

69 ~~precursor~~aerosols (Crutzen, 1970; Shindell et al., 2009; Hoek et al., 2013; Chen et al., 2022). Satellite

70 instruments provide observations of tropospheric NO_2 on a global scale, and they have been extensively

71 used to estimate emissions of nitrogen oxides ($NO_x = NO + NO_2$) (Lin and Mcelroy, 2011; Beirle et al.,

72 2011; Gu et al., 2014; Kong et al., 2022a), surface NO_2 concentrations (Wei et al., 2022; Cooper et al.,

73 2022), trends and variabilities (Richter et al., 2005; Cui et al., 2016; Krotkov et al., 2016; Van Der A et

74 al., 2017), and impacts on human health and environment (Chen et al., 2021).

75 To date, most spaceborne instruments for NO_2 measurements, including the Global Ozone

76 Monitoring Instrument (GOME) (Burrows, 1999), the Ozone Monitoring Instrument (OMI~~,~~) (Levelt et

77 al., 2006), the Global Ozone Monitoring Experiment 2 (GOME-2) ~~and the TROPospheric~~(Callies et al.,

78 2000) and the TROPOspheric Monitoring Instrument (TROPOMI~~,~~) (Veefkind et al., 2012), are mounted

79 on sun-synchronous low Earth orbit (LEO) satellites ~~(Boersma et al., 2011; Richter et al., 2011; Van~~

80 ~~Geffen et al., 2020).~~. These instruments passively measure backscattered radiance from the Earth's

81 atmosphere, and measurements at each ground location are done 1–2 times a day. The Geostationary

82 Environment Monitoring Spectrometer (GEMS) on board the Geostationary Korea Multi-Purpose

83 Satellite-2B (GK-2B) was successfully launched in February 2020. The instrument provides

84 measurements of NO_2 and other pollutants in the daytime on an hourly basis (Kim et al., 2020). It

85 complements LEO satellite observations by providing a more comprehensive picture of the daytime

86 evolution of NO_2.

87 There are three successive stages in the retrieval of tropospheric NO_2 vertical column densities

88 (VCDs) in the UV-Vis range based on satellite observations. The first step is to retrieve total NO_2 slant

89 column densities (SCDs) with spectral fitting techniques, such as the Differential Optical Absorption

90 Spectroscopy (DOAS~~) technique, which provides~~). The SCD represents the abundance of NO_2 along the

91 effective light path from the sun through the atmosphere to the satellite instrument. Next, the

92 contributions from stratospheric NO_2 to the total SCDs are removed in order to obtain tropospheric ~~NO_2~~

93 SCDs. Finally, the tropospheric SCDs are converted to VCDs using calculated air mass factors (AMFs~~,~~

94 ~~which~~). The AMF calculations are highly sensitive to the observation geometry, cloud parameters,

95 aerosols, surface conditions and the shape of the NO_2 vertical distribution. Over polluted areas, errors in

96 the retrieved tropospheric NO_2 VCDs are dominated by the uncertainties in AMF calculations (Boersma

3

97 et al., 2004; Lorente et al., 2016)~~; errors are sensitive to assumptions on~~ associated with aerosol optical

98 effects, surface reflectance~~,~~ and a priori NO$_2$ vertical profiles (Zhou et al., 2010; Lin et al., 2014; Lin et

99 al., 2015; Vasilkov et al., 2016; Lorente et al., 2018; Liu et al., 2019; Liu et al., 2020; Vasilkov et al.,

100 2021).

101 The official GEMS retrieval algorithm for tropospheric NO$_2$ VCDs is developed by Lee et al. (2020).

102 The total NO$_2$ SCDs are retrieved using the DOAS technique~~; they~~. They are then converted to total NO$_2$

103 VCDs by using ~~the~~a precomputed look-up table of box AMFs ~~calculated~~ based on the linearized pseudo-

104 spherical scalar and vector discrete ordinate radiative transfer code (VLIDORT~~).~~) version 2.6. Finally,

105 stratosphere-troposphere separation (STS) is performed to derive tropospheric NO$_2$. Validation results

106 have shown the overall capability of the official GEMS NO$_2$ algorithm~~,~~ (Kim et al., 2023), but several

107 problems are also reported, such as overestimation of total NO$_2$ SCDs and tropospheric NO$_2$ VCDs, and

108 some degree of striping in NO$_2$ retrieval data.

109 In this study, we present a research product which we name as POMINO-GEMS. This product is

110 built upon our Peking University OMI NO$_2$ (POMINO) algorithm which focuses on the tropospheric

111 AMF calculations and has been applied to OMI and TROPOMI (Lin et al., 2014; Lin et al., 2015; Liu et

112 al., 2019; Liu et al., 2020; Zhang et al., 2022). Here we extend the AMF calculation by constructing a

113 hybrid method to estimate tropospheric SCDs for GEMS. The hybrid method makes use of the total

114 SCDs from the official GEMS product, total SCDs and stratospheric VCDs from the official TROPOMI

115 product, as well as hourly ~~variations of~~ stratospheric ~~VCDs~~VCD data from the NASA Global Earth

116 Observing System Composition Forecast (GEOS-~~Chem simulations~~CF) v1 product. We validate our

117 initial set of retrieval results for tropospheric NO$_2$ VCDs in June-July-August (JJA) 2021, by using

118 independent data of tropospheric NO$_2$ from the POMINO-TROPOMI v1.2.2 ~~product~~, OMNO2 v4 and

119 GOME-2 GDP 4.8 products, ground-based and mobile-car MAX-DOAS measurements, and surface

120 concentration observations from the Ministry of Ecology and Environment (MEE) of China. We provide

121 a simplified estimate of retrieval errors in the end.

122 **2. Method and data**

123 **2.1 Construction of POMINO-GEMS retrieval algorithm**

124 Figure 1 shows the flow chart of POMINO-GEMS retrieval algorithm. There are two essential steps.

125 The first is to calculate tropospheric NO$_2$ SCDs on an hourly basis, through fusion of total SCDs from

126 the official GEMS v1.0 L2 NO_2 product, total SCDs and stratospheric VCDs from the TROPOMI PAL

127 v2.3.1 L2 NO_2 product, and diurnal variations of stratospheric NO_2 from ~~nested~~the GEOS-~~Chem (v9-02~~

128 ~~simulations.~~CF v1 product. We then calculate tropospheric NO_2 AMFs to convert SCDs to VCDs.~~Details~~

129 ~~are described in the next sub-sections~~.
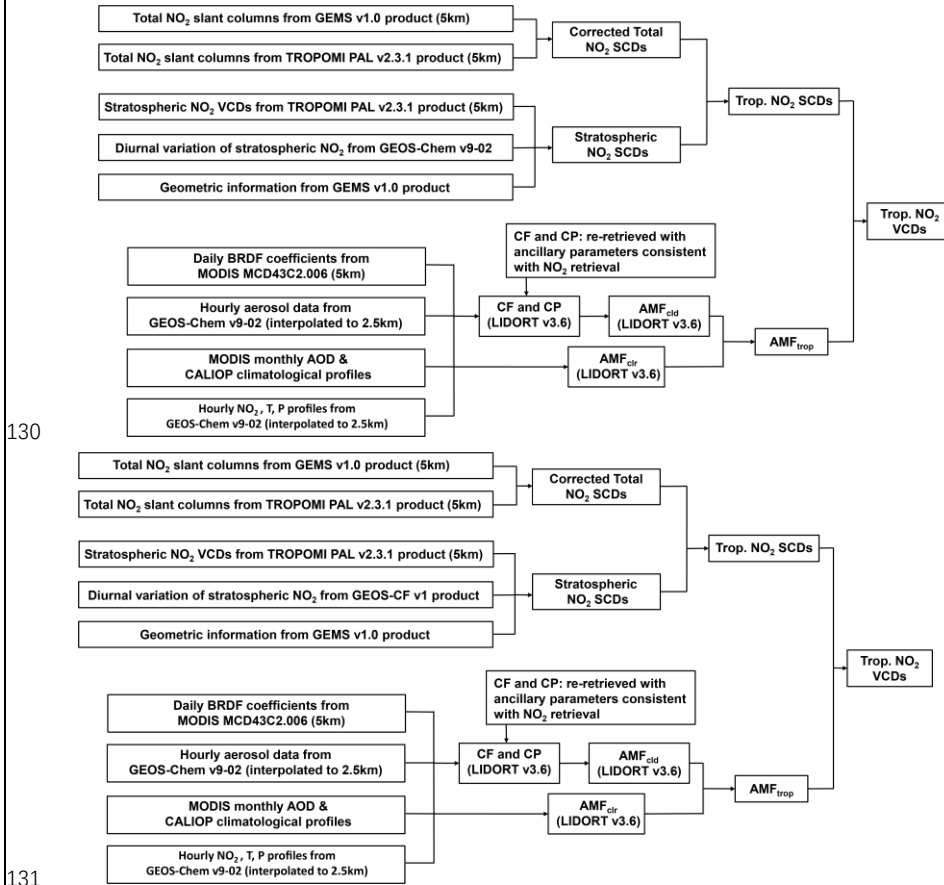
132 **Figure 1. Flow chart of POMINO-GEMS retrieval algorithm. The numbers in the boxes, such as 5 km, refer**

133 **to horizontal resolutions.**

134 **2.1.1 GEMS NO_2 and cloud data**

135 The GEMS instrument is on board the GK-2B satellite locating at 128.2°E over the equator (Kim

136 et al., 2020). The spectral wavelength range of GEMS is 300-500 nm, covering main absorption spectra

137 of aerosols and trace gases. The nominal spatial resolution is typically 7 km × 8 km for gases and 3.5 km

138 × 8 km for aerosols in the eastern and central scan ~~domain~~domains; however, the north-south spatial

5

139 resolution can exceed 25 km in the western side. The whole field of view (FOV) covers about 20 Asian

140 countries within latitudes 5°S to 45°N and longitudes 80°E to 152°E. Given the variation of solar zenith

141 angle (SZA), there are four scan scenarios moving from east to west, including Half East (HE), Half

142 Korea (HK), Full Central (FC) and Full West (FW), moving from east to west.). It takes 30 minutes (for

143 example, 00:45 – 01:15 UTC) for GEMS to scan its full coverage during each measurementscenario,

144 and the next 30 minutes to transmit data to the ground data center. The number of hourly GEMS

145 observations per day varies from 6 in winter to 10 in summer, corresponding to the annual movement of

146 subsolar points relative to the Earth.

147 We take hourly total (stratospheric + tropospheric) NO₂ SCDs from the official GEMS v1.0 L2 NO₂

148 product, and convert them to $0.05° \times 0.05°$ gridded data by means of an area-weighted oversampling

149 technique. We also use continuum reflectancesThe value of each grid cell is the mean value of pixel-

150 based GEMS observations weighted by the ratio of the overlap area of each pixel to the area of grid cell.

151 We also use continuum reflectance data (i.e., spectrally smooth reflectance from molecular and aerosol

152 extinction as well as surface reflectance effects) and O₂-O₂ SCDs from the official GEMS v1.0 L2 cloud

153 product to re-calculate cloud parameters as a prerequisite for tropospheric NO₂ AMF calculations. Details

154 of the GEMS retrievals can be found in the algorithm theoretical basis document (ATBD) (Lee et al.,

155 2020).

156 **2.1.2 TROPOMI, OMI and GOME-2 NO₂ data**

157 The TROPOMI instrument is on board the sun-synchronous satellite Sentinel-5 Precursor, with an

158 Equator overpass time of about 13:30 local solar time (LST) (Van Geffen et al., 2020). It provides

159 measurements for various trace gases, aerosols and cloud properties with a wide spectral range from UV

160 to shortwave infrared. TROPOMI achieves daily global coverage with a full swath width of about 2600

161 km. The horizontal resolution is 3.5 km × 7 km (3.5 km × 5.5 km since 6 August 2019) at nadir, with a

162 maximum width of about 14 km for pixels near the edge of the swath.

163 Table S1 compares the basic information of GEMS with those of TROPOMI, OMI and GOME-2

164 instruments. In this study, TROPOMI data are used for derivation of POMINO-GEMS NO₂ VCDs, and

165 data from all of the three LEO instruments are used for comparison with POMINO-GEMS.

166 We use total NO₂ SCDs and stratospheric NO₂ VCDs from the official TROPOMI PAL v2.3.1 L2

167 NO₂ product, and convert them to $0.05° \times 0.05°$ gridded data, again using an area-weighted oversampling

168 technique. Details of TROPOMI total SCD retrievals and stratospheric VCD calculations are given in

169 the TROPOMI ATBD (Van Geffen et al., 2022a). ~~This intermediate~~The TROPOMI PAL product is

170 reprocessed with TROPOMI NO_2 data processor v2.3.1 for the period from 1 May 2018 to 14 November

171 2021; it will be replaced by the full mission reprocessing with NO_2 processor v2.4.0 in the future (Eskes

172 et al., 2021). The most important improvement in this PAL product ~~over~~upon the previous OFFL v1.3 is

173 the replacement of the FRESCO-S algorithm with the FRESCO-wide cloud retrieval algorithm, which

174 leads to higher, more reasonable cloud pressure (CP) estimates and substantial increases in tropospheric

175 NO_2 VCDs (by 20% – 50%) over polluted regions like Eastern China in winter (Eskes et al., 2021; Van

176 Geffen et al., 2022b).

177 ~~In addition, we use the POMINO-TROPOMI v1.2.2 tropospheric NO₂ VCD product to compare~~

178 ~~with POMINO-GEMS results. The previous POMINO-TROPOMI v1 data show better data~~We use the

179 POMINO-TROPOMI v1.2.2, OMNO2 v4 (Krotkov et al., 2019) and GOME-2 GDP 4.8 (Valks et al.,

180 2019) tropospheric NO_2 VCD products to compare with POMINO-GEMS results. The previous

181 POMINO-TROPOMI v1 data show higher accuracy in polluted situations and improved consistency

182 with MAX-DOAS measurements when compared with the official TM5-MP-DOMINO (OFFLINE)

183 product (Liu et al., 2020). POMINO-TROPOMI v1.2.2 improves upon v1 by (1) using tropospheric NO_2

184 SCD and CP data from the updated TROPOMI PAL v2.3.1 NO_2 product, (2) interpolating the daily NO_2,

185 pressure, temperature and aerosol vertical profiles from nested GEOS-Chem (v9-02) simulations into a

186 horizontal grid of 2.5 km x 2.5 km for subsequent tropospheric AMF calculations, and (3) including

187 several minor bug fixes.

188 **2.1.3 Calculation of total NO_2 SCDs**

189 We select valid satellite pixels following common practice. For the daily POMINO-TROPOMI

190 v1.2.2 L2 NO_2 product, we exclude pixels with SZA or viewing zenith angle (VZA) greater than 80°,

191 high albedos caused by ice or snow on the ground, quality flag values (from the TROPOMI PAL v2.3.1

192 product) less than 0.5 or cloud radiance fraction (CRF) greater than 50%, and then map the valid data to

193 a 0.05° × 0.05 ° grid. For the daily OMNO2 v4 L2 NO_2 product, we exclude pixels with SZA or VZA

194 greater than 80°, with scene Lambert-equivalent reflectivity (LER) greater than 0.3, affected by row

195 anomaly (XTrackQualityFlags is not zero), marked without quality assurance (vcdQualityFlag is not an

196 even integer) or with CRF greater than 50%, and then map the valid data to a 0.25° × 0.25 ° grid. For the

197 daily GOME-2 GDP 4.8 L2 NO_2 product, we exclude pixels with latitude greater than 70°, SZA greater

198 than 80°, failed retrieval (NO2Tropo_Flag is set to 1 or 2) or with CRF greater than 50%, and then map

199 the valid data to a 0.5° × 0.5° grid.

2.1.3 GEOS-CF stratospheric NO_2 data

201   The NASA GEOS-CF system combines the Global Earth Observing System (GEOS) weather

202 analysis and forecasting system with GEOS-Chem v12.0.1 chemistry module (http://geoschem.org) to

203 provide near real-time estimates of atmospheric compositions with daily 5-day forecasts. Detailed

204 information of the model, including chemistry, emissions and deposition, and evaluation of the GEOS-

205 CF tropospheric simulation and forecast skill are presented in Keller et al. (2021). In particular, the

206 GEOS-Chem v12.0.1 chemistry scheme includes online stratospheric chemistry that is fully coupled with

207 tropospheric chemistry through the Unified tropospheric-stratospheric Chemistry eXtension (UCX)

208 mechanism (Eastham et al., 2014). The GEOS-CF stratospheric results are consistent with satellite

209 observations, albeit with notable underestimation of NO_x and HNO_3 in the polar regions (Knowland et

210 al., 2022b).

211   The GEOS-CF outputs have a horizontal resolution of 0.25° × 0.25 °and a temporal resolution of 1

212 hour for NO_2 and other ancillary data used here (Knowland et al., 2022a). We convert instantaneous

213 stratospheric NO_2 volume mixing ratio in dry air at each hour (e.g., 00:00 UTC) into 0.05° × 0.05 °

214 gridded vertical column densities based on estimated tropopause information in GEOS-CF v1. In Section

215 2.1.5, we first evaluate GEOS-CF v1 stratospheric NO_2 VCDs with those of TROPOMI PAL v2.3.1

216 product, and then calculate hourly stratospheric NO_2 VCDs by combining GEOS-CF v1 data for each

217 hour and TROPOMI PAL v2.3.1 stratospheric NO_2 VCD data in the early afternoon.

2.1.4 Calculation of total NO_2 SCDs

219   We use TROPOMI data to correct GEMS total NO_2 SCDs, ~~taking into account potential~~given

220 ~~known~~ issues in GEMS data. ~~Figures~~Specifics for the NO_2 SCD retrieval of TROPOMI PAL v2.3.1 and

221 GEMS v1.0 operational products are provided in Table S2.

222   Figure 2a and b show the spatial distribution of monthly mean total NO_2 geometric column densities

223 (GCDs, calculated as SCDs divided by geometric AMFs) in June 2021 from TROPOMI PAL v2.3.1 and

224 GEMS v1.0, respectively. The horizontal resolution is 0.05° × 0.05 °. The GCDs are used to compare the

225 two products after removing the effect of measurement geometry. Matching for each day between hourly

GEMS observations and the TROPOMI data at the closest observation time is done to ensure temporal compatibility. The figures show that the spatial pattern of GEMS GCDs agrees well with that ~~from~~of TROPOMI, with high values over the North China Plain (NCP) and Northwestern India, as well as major metropolitan clusters such as Seoul and the Yangtze River Delta (YRD). However, there are two systematic problems in GEMS GCDs. ~~Firstly~~First, the GEMS GCD values are abnormally high over the northern and northwestern ~~part~~parts of GEMS FOV, especially over Mongolia, Qinghai, Inner Mongolia, Xinjiang and Tibet of China. ~~Secondly, the~~Second, west-east stripes exist over the whole domain, similar to the spurious across-track variability issue for OMI. This stripe issue exists at all hours (Figure S1). It is likely associated with the specific scan modes of GEMS, as well as periodically occurring bad pixels as one of remaining calibration issues (Boersma et al., 2011; Lee et al., 2023).
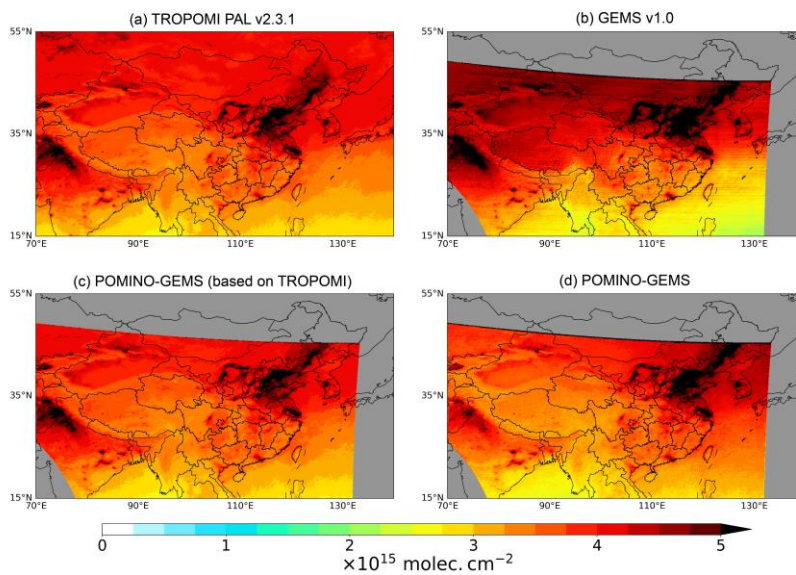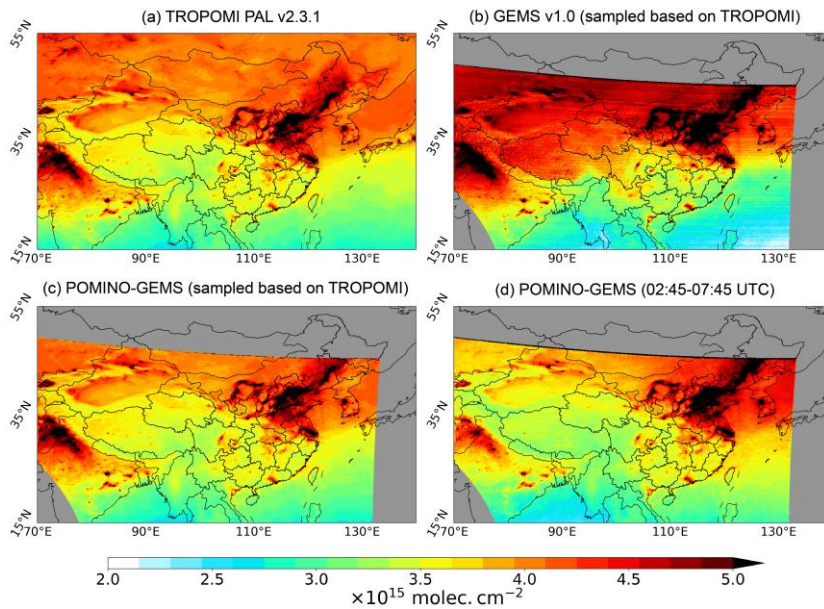
Figure 2. Spatial distribution of monthly mean total NO₂ GCDs on a 0.05° × 0.05 °grid in June 2021. (a) ~~The~~ **TROPOMI PAL v2.3.1 product, (b)** ~~the~~ **official GEMS v1.0 product** ~~, (c)~~ **that spatiotemporally matches with TROPOMI, (c)** ~~the~~ **corrected POMINO-GEMS product that spatiotemporally** ~~match~~**matches with TROPOMI, and (d)** ~~the~~ **corrected POMINO-GEMS product** ~~at all observation hours.~~ **averaged over 02:45 – 07:45 UTC. Note the range of the color bar is 2.0 – 5.0 × 10¹⁵ molec. cm⁻². The regions in grey mean there are no valid observations.**

To correct the two issues in the GEMS official total NO₂ SCD product, we combine GEMS and TROPOMI observations to obtain hourly 0.05° × 0.05 °corrected total NO₂ SCDs for each day using Eqs. (1) and (2):

$$\Delta \text{GCD} = \frac{1}{n} \sum_{i=1}^{n} (\text{GCD}_{\text{total},h_i}^{\text{TROPOMI}} - \text{GCD}_{\text{total},h_i}^{\text{GEMS}}) \tag{1}$$

$$\text{SCD}_{\text{total},h}^{\text{corrected}} = \text{SCD}_{\text{total},h}^{\text{GEMS}} + \Delta \text{GCD} \times \text{AMFgeo}_{h}^{\text{GEMS}} \tag{2}$$

In Eqs. (1) and (2), index h represents the hour of GEMS observations on each day; h_i the hour when both GEMS and TROPOMI have valid observations for the same grid cell; and n the number of h_i. The value of n is 1 or 2 depending on the overpass times of TROPOMI. There are two steps in the correction process. ~~Firstly~~First, we calculate a geometry-independent correction map for each day using total NO₂ GCDs from GEMS and TROPOMI that match spatially and temporally (Eq. (1)). We use the absolute difference instead of a scaling factor as a simple correction. We then apply the correction to the

10

带格式的: 左

original GEMS total NO$_2$ SCDs at each hour on the same day, ~~by accounting for~~with the diurnal variation in AMF associated with measurement geometry <u>accounted for</u> (Eq. (2)).

<u>In Eq. (2), we implement a simple geometric correction (concerning SZAs and VZAs) for AMFs instead of using the actual AMFs; the latter could account for the differences in relative azimuth angles and other factors. Specific derivation of this assumption is given in Section 1 of the Supplement Information (SI). The correction is assumed to be acceptable with an extra uncertainty introduced to the total NO$_2$ SCDs, as will be further discussed in Section 3.5.</u>

Figure 2c shows <u>the</u> monthly mean corrected POMINO-GEMS total NO$_2$ GCDs in June 2021 after spatial and temporal matching with TROPOMI. The corrected GCD values in <u>the</u> northern GEMS FOV are much reduced compared with those in the original GEMS data. Moreover, most stripe-like patterns are removed in the corrected GCDs.

Figure 2d is similar to Fig. 2c but for GCDs averaged ~~at all observation hours~~ <u>over 02:45 – 07:45 UTC</u> in June 2021. <u>Figure S3 further compares the original GEMS and POMINO-GEMS total NO$_2$ GCDs at each hour in JJA 2021, showing similar improvements as well.</u> The differences between ~~Figures~~<u>Figure</u> 2c and ~~2d~~<u>d</u> indicate the influence of different sampling ~~times as well as the limitation of~~<u>hours combined with the</u> daily correction map. Specifically, the correction value of each grid cell is calculated at the specific hour when both GEMS and TROPOMI have valid observations, but this value is applied to original GEMS SCDs at all hours.

<u>Our correction method is done for each grid cell. We tested other correction methods by applying the same correction value to grid cells within a 20° × 20 ° domain, at the same latitude, or at the same longitude. These alternative methods can reduce the high bias over the northern and northwestern GEMS FOV to various extents, but cannot remove the stripes (not shown). We also note that our simple correction is a temporary solution before the aforementioned systematic problems in the official GEMS SCD retrieval are solved by improving spectral fitting. In Sections 3.3 and 3.4, we compare the diurnal variations of tropospheric NO$_2$ VCDs based on corrected and uncorrected GEMS SCDs.</u>

2.1.~~4~~<u>5</u> Calculation of stratospheric and tropospheric NO$_2$ SCDs

We construct a dataset of hourly stratospheric NO$_2$ SCDs at 0.05° × 0.05 °by using TROPOMI <u>PAL v2.3.1</u> stratospheric NO$_2$ VCDs, diurnal variation of stratospheric NO$_2$ VCDs provided by GEOS-~~Chem simulations~~<u>CF v1 product</u>, and GEMS geometric AMFs. ~~Nested~~

11

284 Figure S4 shows the comparison results between GEOS-~~Chem v9-02 simulations for Asia at~~CF v1

285 and TROPOMI PAL v2.3.1 stratospheric NO_2 VCDs in June 2021. Consistent spatial and temporal

286 sampling is done. N is the total number of matched 0.~~25° lat.~~05° × 0.~~3125° long.~~05° grid cells. The

287 stratospheric VCDs from both products vary in the range of $2 - 5 \times 10^{15}$ molec. cm^{-2}, with ~~47 vertical~~

288 ~~layers are driven with daily~~spatiotemporal correlation of 0.99, linear regression slope of 0.99 and

289 normalized mean bias (NMB) of 0.02%. This consistency provides confidence on the overall reliability

290 of GEOS-~~FP meteorological fields; see details in our previous studies (Lin et al., 2014; Lin et al., 2015).~~

291 ~~We add the simulated NO_2 sub-columns within layers 37 to 43 (roughly above 17 km) to represent NO_2~~

292 ~~VCDs in the stratosphere.~~ CF stratospheric NO_2 data.

293 First, we calculate stratospheric NO_2 VCDs at a reference hour for each day using Eqs. (3) and (4):

294 $$\text{ratio}_{h_0}^h = \frac{\text{VCD}_{\text{strat},h}^{\text{GC}}}{\text{VCD}_{\text{strat},h_0}^{\text{GC}}} \tag{3}$$

$$\text{ratio}_{h_0}^h = \frac{\text{VCD}_{\text{strat},h}^{\text{GEOS-CF}}}{\text{VCD}_{\text{strat},h_0}^{\text{GEOS-CF}}}$$

295 $$\text{VCD}_{\text{strat},h_0} = \frac{1}{n}\sum_{i=1}^{n}\frac{\text{VCD}_{\text{strat},h_i}^{\text{TROPOMI}}}{\text{ratio}_{h_0}^{h_i}} \tag{4}$$

296 Here, Eq. (3) defines the ratio of GEOS-~~Chem simulated~~CF stratospheric NO_2 at hour h to that at

297 the reference hour h_0, which is chosen to be ~~00~~01:00 UTC (Figure ~~S1~~S5). In Eq. (4), h_i represents the

298 observation time of every TROPOMI orbit that overlaps with GEMS FOV, and n the number of h_i for

299 each grid cell.

300 Second, we use the ratio from a given time h to h_0 and stratospheric NO_2 VCDs at h_0 to derive

301 stratospheric NO_2 VCDs at h for each day (Eq. (5)).

302 $$\text{VCD}_{\text{strat},h} = \text{VCD}_{\text{strat},h_0} \times \text{ratio}_{h_0}^h \tag{5}$$

303 Figure 3 shows the derived monthly mean stratospheric NO_2 VCDs at each hour in June 2021 on a

304 0.05° × 0.05 ° grid. ~~The spatial patterns are very similar at different times, indicating weak simulated~~

305 ~~diurnal variation of stratospheric NO_2 in summer. There is a strong meridional gradient of stratospheric~~

306 ~~NO_2, with the higher values in the north associated with longer lifetimes.~~ The abrupt decease of

307 stratospheric NO_2 VCDs after sunrise is caused by resumed photochemical conversion of NO_2 to NO (Li

308 et al., 2021b). There is a strong meridional gradient of stratospheric NO_2 in the daytime, with the higher

309 values in the north associated with longer lifetimes. The stratospheric NO_2 increase quasi-linearly during

310 the daytime; linear regression to the mean stratospheric NO_2 VCDs over the whole domain from 01:45

311 to 07:45 UTC results in an increasing rate of $(1.12\pm0.03) \times 10^{14}$ molec. cm^{-2} h^{-1}. This result is consistent

314 Finally, we use GEMS geometric AMFs to convert the stratospheric NO$_2$ VCDs to SCDs at each

315 hour, and then subtract them from the total SCDs to obtain tropospheric SCDs (Eqs. (6) and (7)). In the

316 stratosphere, the geometric AMFs are essentially the same as the actual AMFs

317
$$SCD_{strat,h} = VCD_{strat,h} \times AMFgeo_h^{GEMS} \tag{6}$$

318
$$SCD_{trop,h}^{GEMS*} = SCD_{total,h}^{corrected} - SCD_{strat,h} \tag{7}$$

319
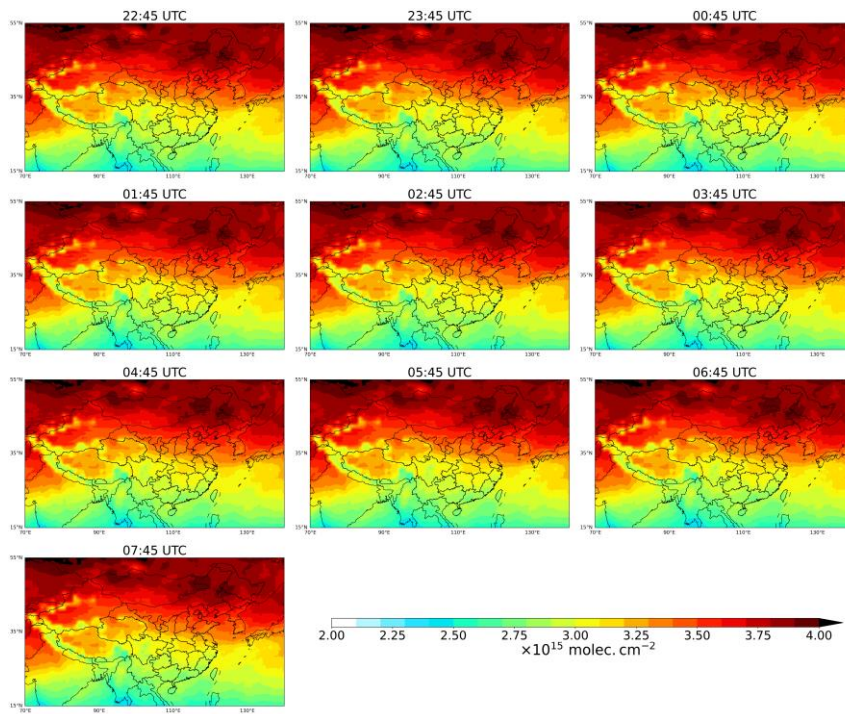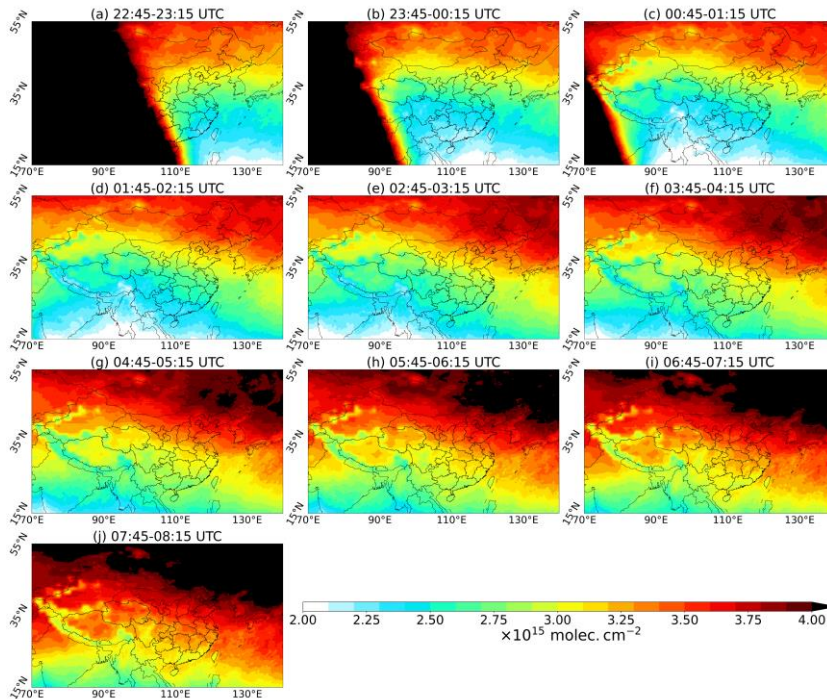
Figure 3. Spatial distribution of POMINO-GEMS derived monthly mean stratospheric NO₂ VCDs at each hour on a 0.05° × 0.05 °grid in June 2021. Note the range of the color bar is 2.0 – 4.0 × 10¹⁵ molec. cm⁻².

2.1.~~5~~6 Calculation of tropospheric AMFs

~~For tropospheric AMF calculations (Figure 1), we use a parallelized LIDORT-driven AMFv6 package~~Tropospheric NO₂ AMF is dependent on three factors as defined in Palmer et al. (2001): the viewing geometry, the scattering weights describing the sensitivity of the backscattered spectrum to the abundance of the absorber, and a priori NO₂ vertical profile (Eq. (8)).

$$\mathrm{AMF} = \mathrm{AMF_G} \int_0^{z_\mathrm{T}} w(z) S(z) \mathrm{d}z \qquad (8)$$

In Eq. (8), $\mathrm{AMF_G}$ is the geometric AMF and a function of SZA and VZA, $w(z)$ the scattering weight at altitude z, $S(z)$ the normalized vertical profile of NO₂ number density, and z_T the tropopause. Following Yang et al. (2023), we refer to $\int_0^{z_\mathrm{T}} w(z) S(z) \mathrm{d}z$ as the scattering correction factor for discussion in Section 3.2. For tropospheric AMF calculations (Figure 1), we use a parallelized AMFv6 package driven by LIDORT version 3.6; this is similar to the one used in our previous POMINO products (Lin et al., 2014; Lin et al., 2015; Liu et al., 2019) but with modifications to adapt to the geostationary observing

characteristics and high spatiotemporal resolution of GEMS. We take daily BRDF coefficients with a horizontal resolution of 5 km from the MODIS MCD43C2.006 dataset ~~(Lucht et al., 2000; Lin et al., 2014; Lin et al., 2015; Liu et al., 2020) to account for the anisotropy of surface reflectance (Zhou et al., 2010). Hourly-varying aerosol parameters, a priori NO$_2$ profiles as well as temperature~~(Lucht et al., 2000) to account for the anisotropy of surface reflectance over land and coastal ocean regions , and OMLER v3 albedo over open ocean (Zhou et al., 2010; Lin et al., 2014; Liu et al., 2020). Hourly-varying aerosol parameters, a priori NO$_2$ profiles, temperature profiles and pressure profiles are interpolated from nested GEOS-Chem (v9-02) results to a horizontal resolution of 2.5 km, using the Piecewise Cubic Hermite Interpolating Polynomial (PCHIP) method. Furthermore, we deploy AOD observations from the MODIS/Aqua Collection 6.1 MYD04_L2 dataset ~~(Lin et al., 2014; Lin et al., 2015; Liu et al., 2019; Liu et al., 2020)~~ to constrain model-simulated AOD on a monthly basis~~.~~ (Lin et al., 2014; Lin et al., 2015; Liu et al., 2019; Liu et al., 2020); and we use a self-constructed monthly climatological dataset of aerosol extinction profiles based on CALIOP L2 data over 2007-2015 to constrain modeled aerosol vertical profiles on a monthly climatology basis (Liu et al., 2019). We re-retrieve cloud parameters based on O$_2$-O$_2$ SCDs and continuum reflectances from the official GEMS v1.0 cloud product, using ancillary parameters consistent with those used in NO$_2$ AMF calculations. Instead of relying on a look-up table (LUT), we conduct pixel-by-pixel radiative transfer calculations with the parallelized AMFv6 package. The independent pixel approximation (IPA) is assumed for cloud-contaminated pixels as in other algorithms. Finally, we use the AMF data to convert tropospheric NO$_2$ SCDs to VCDs.

Invalid pixels in the POMINO-GEMS product are filtered based on the following criteria. We exclude pixels with ~~solar zenith angle (~~SZA~~)~~ or ~~viewing zenith angle (~~VZA~~)~~ greater than 80°, or with the ground covered by ice or snow. To minimize cloud contamination, we exclude pixels with ~~cloud radiance fractions (~~CRF~~)~~ greater than 50~~% in the POMINO-GEMS product.~~%.

2.2 Estimation of surface NO$_2$ concentrations

In order to validate satellite NO$_2$ products with surface concentration measurements from MEE, we convert tropospheric NO$_2$ VCDs from satellite products on a 0.05° × 0.05 ° grid to surface NO$_2$ mass concentrations using GEOS-Chem simulated NO$_2$ vertical profiles and the box heights of the lowest model layer (Eq. (~~8~~9)).

$$C_{\text{surf}} = \text{VCD}_{\text{trop}}^{\text{SAT}} \times R^{\text{GC}} \times \frac{M}{N \times H^{\text{GC}}} \times 2 \qquad (9)$$

In Eq. (89), C_{surf} represents the estimated surface NO$_2$ mass concentration in µg m^{-3}, $\text{VCD}_{\text{trop}}^{\text{SAT}}$ the satellite tropospheric VCD in molec molecules. m^{-2}, R^{GC} the GEOS-Chem simulated hourly ratio of NO$_2$ sub-column in the lowest layer to the total tropospheric column, M the NO$_2$ molar mass in µg mol^{-1}, N the Avogadro constant, and H^{GC} the box height of the lowest layer in m. The thickness of the lowest layer of GEOS-Chem (about 130 m) is too large for the layer average NO$_2$ mass concentration to represent that near the ground (Liu et al., 2018)(Liu et al., 2018a); thus the derived concentration is multiplied by a factor of 2 to roughly account for the vertical gradient from the height of ground instrument to the center of the model layer. However, the constant correction factor of 2 neglects the diurnal variation of NO$_2$ vertical gradient, which is related to the diurnal variation of planetary boundary layer (PBL) heights. This issue is discussed in detail in Section 3.4.

2.3 Ground-based MAX-DOAS measurements

We use ground-based MAX-DOAS measurements to validate the POMINO-GEMS and POMINO-TROPOMI v1.2.2 NO$_2$ products (Figure S2). The types, geolocations and observation times of MAX-DOAS stations are summarized in Table 1. Details of each site are described in supplement information (SI).

Table 1. MAX-DOAS measurements

Site name	Type	Geolocation	Measurement time
Fudan University	Urban	121.52°E, 31.34°N	1 June – 31 August 2021
Xuzhou	Suburban	117.14°E, 34.22°N	1 June – 31 August 2021
Hefei	Suburban	117.16°E, 31.91°N	1 June – 30 June 2021
Nanhui	Suburban	121.80°E, 31.06°N	1 June – 31 August 2021
Chongming	Suburban	121.82°E, 31.50°N	1 June – 31 August

			2021
Dianshan Lake	Suburban	120.98°E, 31.30°N	1 June – 31 August 2021
Xianghe	Suburban	116.96°E, 39.75°N	1 June – 31 August 2021
Fukue	Remote	128.68°E, 32.75°N	1 June – 31 August 2021
Cape Hedo	Remote	128.25°E, 26.87°N	1 June – 31 August 2021

381

382   We use ground-based MAX-DOAS NO$_2$ measurements, together with POMINO-TROPOMI v1.2.2,

383   OMNO2 v4 and GOME-2 GDP 4.8 NO$_2$ products, to validate the POMINO-GEMS retrieval results. The

384   types, geolocations and observation times of MAX-DOAS stations are summarized in Table S3, and the

385   location of each site is shown in Figure S6. Details of each site are described in Section 2 of the SI.

386   Kanaya et al. (2014) and Hendrick et al. (2014) have discussed the error in MAX-DOAS NO$_2$ retrieval:

387   uncertainties from a priori aerosol and NO$_2$ profiles are the largest source by 10% – 14%, and the total

388   retrieval uncertainty is typically 12% – 17%.

389   To ensure sampling consistency in time, we average all valid MAX-DOAS measurements within

390   each observation period of GEMS (i.e., 30 minutes) for hourly comparison, and within $\pm$1.5 h of

391   TROPOMI, OMI and GOME-2 overpass time for daily comparison. Following the ~~procedure~~procedures

392   in previous studies (Lin et al., 2014; Liu et al., 2020), we exclude all matched MAX-DOAS data for

393   which the standard deviation exceeds 20% of the mean value to minimize the influence of local events.

394   To ensure sampling consistency in space, we select valid satellite pixels within 5 km of MAX-DOAS

395   sites ~~and conduct spatial averaging. The Grubbs statistical test is performed to exclude outliers in both~~

396   ~~MAX-DOAS and satellite data before comparison.~~for POMINO-GEMS and POMINO-TROPOMI

397   v1.2.2, 25 km for OMNO2 v4 and 50 km for GOME-2 GDP 4.8, and conduct spatial averaging. The

398   Grubbs statistical test, which is used to detect outliers in a univariate data set assumed to exhibit normal

399   distribution (Grubbs, 1950), is performed to exclude outliers in both MAX-DOAS and satellite data

400   before comparison. Only one data pair from Fudan University site is identified as an outlier and removed

401 (Figure S7), and we get 1348 matched hourly data pairs in total.

402 **2.42.4 Mobile-car MAX-DOAS measurements**

403 We use tropospheric NO_2 VCDs from mobile-car MAX-DOAS measurements performed by the
404 Chinese Academy of Meteorological Sciences (CAMS) in the Three Rivers' Source region in July 2021
405 (Cheng et al., 2023). The Three Rivers' Source region is on the northeastern Tibetan Plateau in western
406 China, which is isolated from massive anthropogenic activities, and hence a good place for observations
407 of atmospheric compositions in the background atmosphere. The field campaign lasted from 18th to 30th
408 July 2021 and included four closed-loop journeys, beginning from the meteorological bureau of the city
409 of Xining (the Capital of Qinghai Province) to the meteorological bureau of Dari County of the Guoluo
410 Tibetan Autonomous Prefecture, to the meteorological bureau of Yushu Tibetan Autonomous Prefecture,
411 and then back to Xining City (Figure S6). The spectral analysis of the measurement spectra in the fitting
412 window of 400-434 nm was implemented with the DOAS method. Sequential Fraunhofer reference
413 spectrum (FRS) is used to derive NO_2 differential slant column densities (DSCDs), which are then
414 converted to VCDs by adopting the geometric approximation method. The errors are estimated to be less
415 than 20% at high altitudes. More detailed descriptions of instrumentation, field campaign and data
416 retrieval are in Cheng et al. (2023).

417 We average all valid mobile-car MAX-DOAS measurements within each observation period of
418 GEMS in each $0.05° \times 0.05°$ grid cell, to ensure spatiotemporal consistency. Over relatively clean areas
419 with little human influence and biomass burning such as the Three Rivers' Source region, a large portion
420 of NO_2 is located in the middle and upper troposphere, which is not accounted for in the mobile-car data
421 via such a DSCD-based retrieval method. Indeed, Cheng et al. (2023) showed that the official TROPOMI
422 NO_2 VCDs are higher than mobile-car data by about 40%. Considering that the diurnal variation of
423 middle and upper tropospheric NO_2 is much smaller than that in the lower troposphere, we focus on the
424 correlation of NO_2 diurnal variation between POMINO-GEMS and mobile car MAX-DOAS data.

425 **2.5 Ground-based MEE NO_2 measurements**

426 We use hourly surface NO_2 mass concentration measurements from the MEE air quality monitoring
427 network (https://quotsoft.net/air/). By 2021, more than 2000 MEE stations across China have been
428 established, providing hourly observations for NO_2 and five other air pollutants. Most stations are in

urban or suburban areas. ~~We filter the MEE sites for comparison with satellite data using mean surface-to-total ratios of NO₂ (R^{GC}) in June-July-August 2021 defined in section 2.2. The spatial distribution of R^{GC} is shown in Figure S3a. Only MEE sites at the grid cells where the surface-to-total ratio is larger than the 95th-percentile across all grid cells within the GEMS domain (i.e., 0.12) are included; this results in 855 valid MEE sites, as shown in Figure S3b.~~

The spatial distribution of all MEE sites in the GEMS FOV is shown in Figure S8a, and that of MEE sites over urban, suburban and rural regions are shown in Figure S8b–d, respectively. The classification of sites is based on Tencent user location data with a horizontal resolution of $0.05° \times 0.05°$ for every 0.5 second from 31 August to 30 September 2021 (Figure S8e), adopted from previous work (Kong et al., 2022a). Here, urban MEE sites are defined as where the mean location request times is larger than 50 times per second, suburban sites refer to 5-50 times per second, and rural sites refer to less than 5 times per second. The number of sites for urban, suburban and rural sites are 808, 554 and 71, respectively.

At MEE sites, molybdenum catalyzed conversion from NO₂ to NO and subsequent chemiluminescence measurement of NO is done to estimate NO₂ concentrations. The heated molybdenum catalyst has low chemical selectivity, leading to strong interference from other oxidized nitrogen species such as nitric acid (HNO_3) and peroxyacetyl nitrate (PAN). Therefore, MEE data tend to overestimate the actual NO₂ concentrations, with the extent of overestimation about $10\% - 50\%$ (Boersma et al., 2009; Liu et al., 2018a). The overestimation is dependent on the oxidation level of NO_x, but is currently unclear for each site and hour.

To compare with satellite-derived surface NO₂ concentration data, we average over all valid MEE sites in each $0.05° \times 0.05°$ grid cell to generate gridded MEE NO₂ data for each hour. To ensure sampling consistency for each day, we average MEE observations ~~for~~at two consecutive hours to match GEMS hourly observations – for example, we match the mean value of MEE NO₂ concentrations in 13:00 – 14:00 and 14:00 – 15:00 local solar time (LST) with the GEMS NO₂ in 13:45 – 14:15 LST. We also match MEE observations over the period 13:00 – 14:00 LST with TROPOMI-derived and OMI-derived surface NO₂, and 9:00 – 10:00 LST with GOME-2-derived surface NO₂.

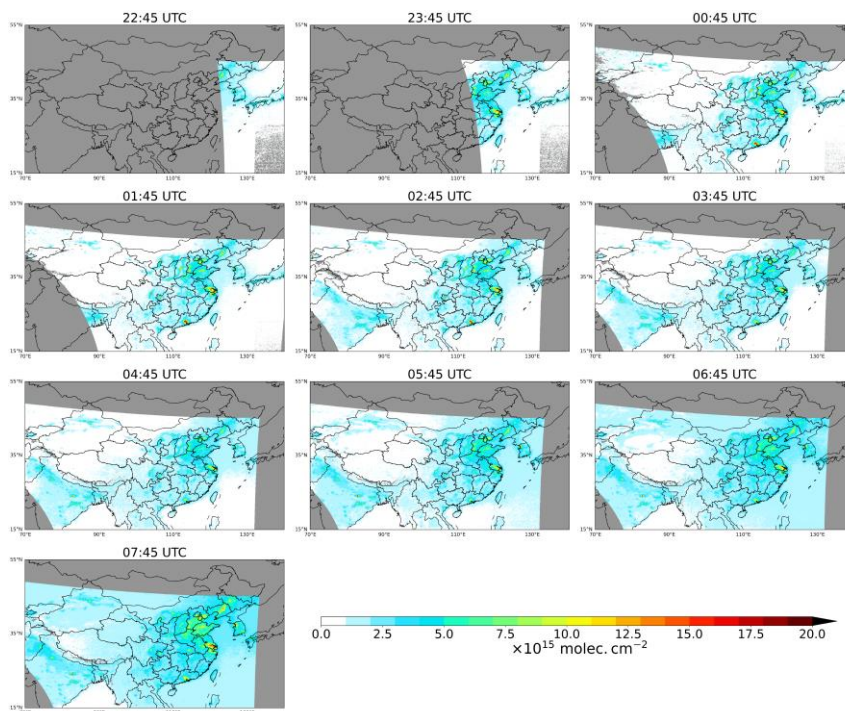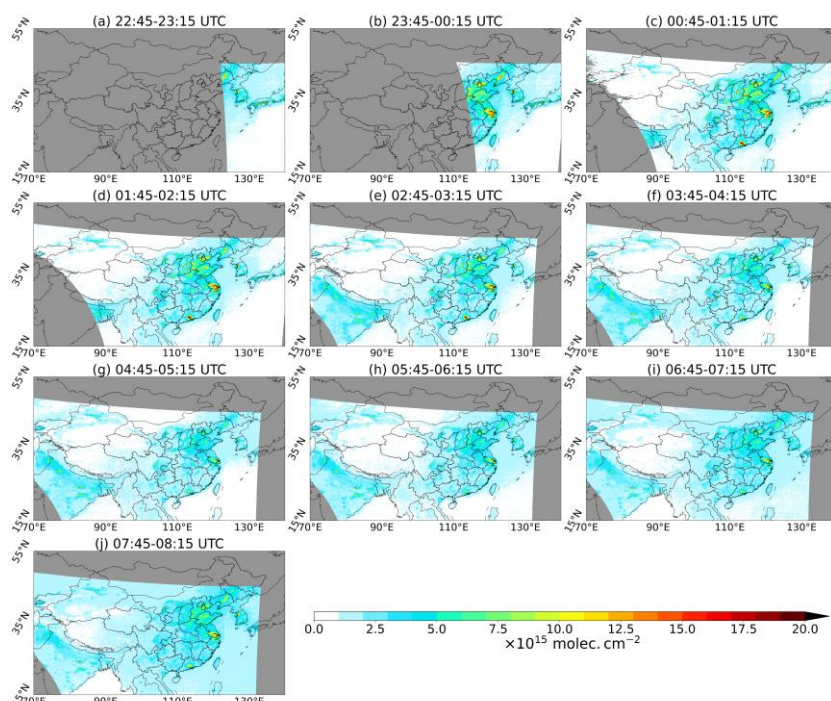**3. Results and discussion**

3.1 POMINO-GEMS tropospheric NO₂ VCDs

Figure 4 shows mean POMINO-GEMS tropospheric NO₂ VCDs at each hour on a $0.05° \times 0.05°$

458 grid in JJA 2021. High values of tropospheric NO_2 columns (> 10×10^{15} molec. cm^{-2}) are evident over

459 populous regions such as South Korea, central and eastern China, and northern India. Clear hotspot

460 signals reveal intense NO_x emissions over city clusters such as Beijing-Tianjin-Hebei (BTH), Yangtze

461 River Delta (YRD), Pearl River Delta (PRD) and Seoul Metropolitan Area (SMA), as well as isolated

462 megacities such as Osaka and Nagoya in Japan, Chengdu and Urumqi in China, and New Delhi in India.

463 Tropospheric NO_2 VCDs are much lower (< 1×10^{15} molec. cm^{-2}) over most of western China and the

464 open ocean, due to low anthropogenic and natural emissions.

465

Figure 4. Spatial distribution of POMINO-GEMS tropospheric NO$_2$ VCDs at each hour on a 0.05° × 0.05° grid in JJA 2021. The regions in grey mean there are no valid observations.

~~Figures 5 presents~~Figure 5a-c present NO$_2$ VCDs in the morning, noon and afternoon in JJA 2021 for eastern China. Data are averaged ~~from~~in 22:45–_01:45 UTC (06:45–_09:45 Beijing Time, BJT), 02:45–_04:45 UTC (10:45–_12:45 BJT) and 05:45–_07:45 UTC (13:45–_15:45 BJT) to represent the morning, noon and afternoon, respectively. In the morning (Figure 5a), there are clear city signals with high NO$_2$ values, reflecting abundant NO$_x$ emissions from traffic. The spatial gradients of NO$_2$ from urban centers to outskirts are very strong. However, these spatial gradients are greatly reduced in the noon and afternoon (Figure 5b and c). For example, the differences of tropospheric NO$_2$ VCDs between the urban center of Xi'an (108.93°N, 34.27°E) and its surrounding areas (within 50 km) are reduced from about 8 × 10^{15} molec. cm^{-2} in the morning to about 4 × 10^{15} molec. cm^{-2} at noon, and then to below 2 × 10^{15} molec. cm^{-2} in the afternoon. This is likely due to chemical loss of traffic-associated NO$_2$, increased emissions from other sectors (e.g., industry), and/or enhanced horizontal transport smearing the spatial gradient.

481

482
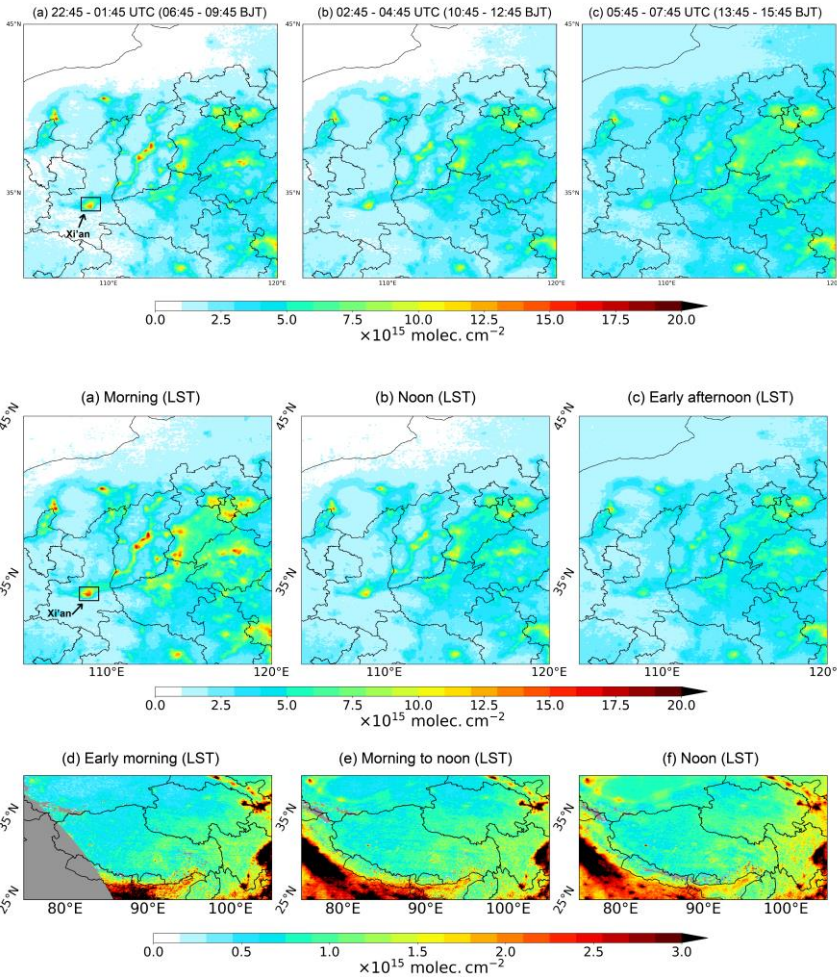
Figure 5. Spatial distribution of three-hour-mean POMINO-GEMS tropospheric NO₂ VCDs in JJA 2021 on a 0.05° × 0.05 °grid over. The first row is for eastern China in the (a) morning, (22:45 – 01:45 UTC), (b) noon (02:45 – 04:45 UTC) and (c) afternoon in JJA 2021. (05:45 – 07:45 UTC). The second row is for western China in the (d) early morning (00:45 – 01:45 UTC), (e) morning to noon (02:45 – 04:45 UTC) and (f) noon (05:45 – 07:45 UTC). The regions in grey mean there are no valid observations.

Over western China with low tropospheric NO₂ VCDs (Figure ~~6~~5d-f), there is a ~~roughly~~ ~~monotonic~~gradual increase of tropospheric NO₂ by about 1×10^{15} molec. cm^{-2} ~~within daily GEMS~~ ~~observations.~~from the early morning to noon. This increase is likely dominated by biogenic NO$_x$ emissions that are sensitive to sunshine intensity and surface temperature (Kong et al., 2022b; Weng et

带格式的: 下标

22

492   al., 2020; Kong et al., 2023). Future studies are needed to understand the exact causes.
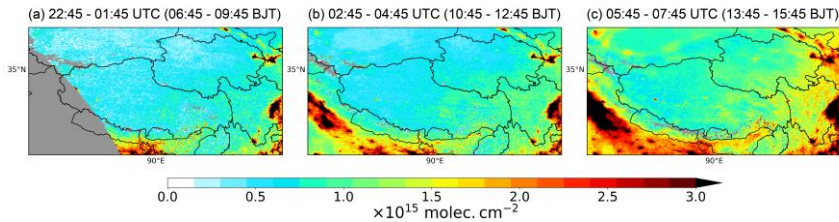
493
494   **Figure 6. Spatial distribution of three-hour-mean POMINO-GEMS tropospheric NO$_2$ VCDs on a 0.05° ×**
495   **0.05° grid over western China in JJA 2021. The local solar time in this region is 1-3 hours earlier than**
496   **Beijing Time.**

497   Figure 6 shows the diurnal variation of POMINO-GEMS tropospheric NO$_2$ VCDs over six different
498   region groups in the GEMS FOV. The six groups are defined based on the levels of mean POMINO-
499   GEMS tropospheric NO$_2$ VCDs at 12:00 LST in JJA 2021 (VCD$_{12:00\ LST}$), and their spatial distributions
500   are also shown in each panel. We convert the observation time from UTC to LST for each time zone in
501   this domain (+5 time zone: 70°E – 82.5° E; +6 time zone: 82.5°E – 97.5°E; +7 time zone: 97.5°E –
502   112.5°E; +8 time zone: 112.5°E – 127.5°E; +9 time zone: 127.5°E – 140°E), and show the NO$_2$ diurnal
503   variations in each time zone with different colors. For low NO$_2$ situations (VCD$_{12:00\ LST}$ ≤ 2 × 10^{15} molec.
504   cm^{-2}), NO$_2$ grow in the morning time in +5 and +6 time zones but not in other time zones. Over high
505   NO$_2$ situations (VCD$_{12:00\ LST}$ > 8 × 10^{15} molec. cm^{-2}, in cities and suburban areas), NO$_2$ in all time zones
506   exhibit a minimum around noontime and a morning peak at 09:00 – 10:00 LST, consistent with previous
507   findings for specific polluted locations (Boersma et al., 2008; Boersma et al., 2009; Li et al., 2021a;
508   Ghude et al., 2020; Herman et al., 2019; Biswas and Mahajan, 2021). In all groups and time zones,
509   tropospheric NO$_2$ VCDs grow from noon to the afternoon.

510   The NO$_2$ diurnal variations are related to multiple driving factors. Different sources with distinctive
511   diurnal patterns dominate the NO$_x$ emissions over different regions. Lightning and biogenic activities are
512   the major emission sources over low NO$_2$ land areas, and they tend to intensify with temperature and
513   radiation in the daytime. Anthropogenic emissions are dominant over polluted cities and suburban areas,
514   where the traffic emissions tend to peak in the mid-morning and late afternoon (Jing et al., 2016; Liu et
515   al., 2018b; Naiudomthum et al., 2022). In addition, the photochemistry plays an important role. NO$_2$ is
516   in chemical balance with NO, and the ratio of NO$_2$ and NO depends on radiation, ozone and peroxyl
517   radicals. NO$_x$ is oxidized to nitric acid and organic nitrates by radicals in the daytime, the level of which

23

depends on radiation, ozone and volatile organic compounds. Thus the lifetime of NO_2 reaches the minimum value around noon, i.e., a few hours in summer. Furthermore, atmospheric transport also affects the diurnal variation of NO_2 at high-value places (e.g., cities) and their surroundings. Further studies are needed to determine the exact causes of NO_2 diurnal variations at individual places.
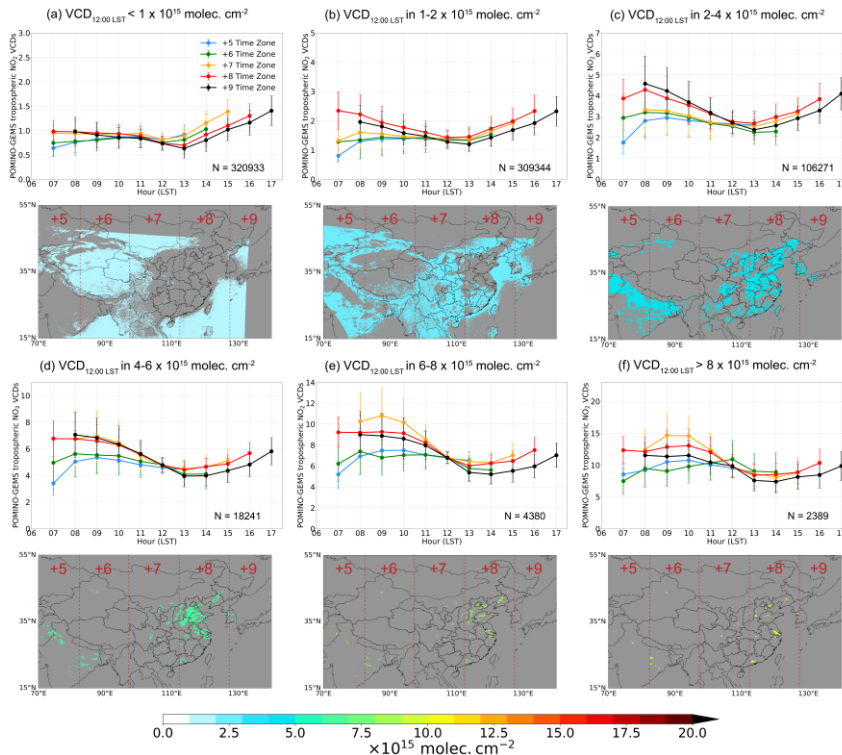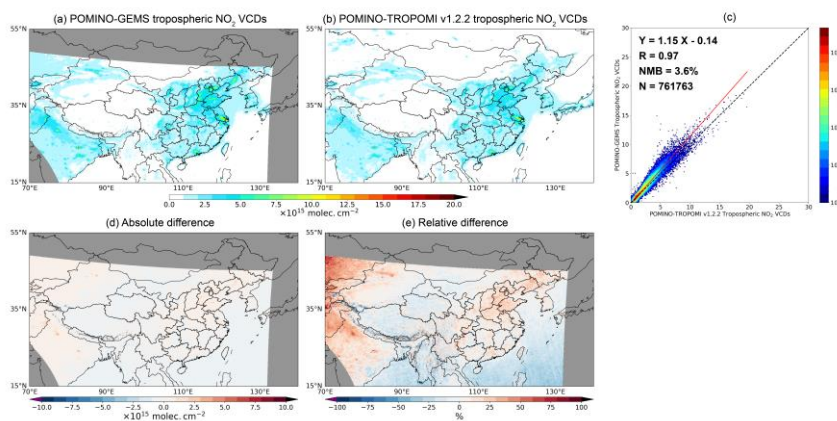

Figure 6. POMINO-GEMS NO_2 diurnal variations for six region groups classified based on mean POMINO-GEMS tropospheric NO_2 VCDs at 12:00 LST in JJA 2021 ($VCD_{12:00\ LST}$). (a) $VCD_{12:00\ LST}$ less than 1×10^{15} molec. cm^{-2}; (b) $VCD_{12:00\ LST}$ in $1 - 2 \times 10^{15}$ molec. cm^{-2}; (c) $VCD_{12:00\ LST}$ in $2 - 4 \times 10^{15}$ molec. cm^{-2}; (d) $VCD_{12:00\ LST}$ in $4 - 6 \times 10^{15}$ molec. cm^{-2}; (e) $VCD_{12:00\ LST}$ in $6 - 8 \times 10^{15}$ molec. cm^{-2} and (f) $VCD_{12:00\ LST}$ larger than 8×10^{15} molec. cm^{-2}. In each panel, different colors denote the NO_2 diurnal variation in different time zones. N denotes the total number of valid $0.05° \times 0.05°$ grid cells in each region. The error bars denote the standard deviation of tropospheric NO_2 VCDs at each hour in each time zone.

3.2 Comparison with POMINO-TROPOMI v1.2.2 ~~NO₂ product~~, OMNO2 v4 and GOME-2 GDP 4.8 NO_2 VCD products

~~Figures~~Figure 7a and b show the POMINO-GEMS and POMINO-TROPOMI v1.2.2 tropospheric NO_2 VCDs, respectively, on a $0.05° \times 0.05°$ grid averaged over JJA 2021. Cloud screening is

24

534   implemented based on the CRFs from each product. To ensure temporal compatibility, matching between

535   hourly GEMS observations and the TROPOMI data at the closest observation time is done for each day.

536   Overall, POMINO-GEMS agrees well with POMINO-TROPOMI with a spatial correlation coefficient

537   of 0.~~97~~98, a linear regression slope of 1.~~15~~18 and a small positive ~~normalized mean bias (~~NMB~~)~~ of ~~3.6~~4.9%

538   (Figure 7c). Regionally, POMINO-GEMS VCDs are higher than those of POMINO-TROPOMI v1.2.2

539   over eastern China, most India and northwestern GEMS FOV, but smaller over western China and the

540   oceans (Figure 7a, b; see Figure S9c and d for differences plots). These differences are related to

541   tropospheric NO_2 AMFs and SCDs. Detailed discussion is given in Section 3 of the SI.

542

(a) POMINO-GEMS tropospheric NO₂ VCDs (sampled based on POMINO-TROPOMI v1.2.2)

(b) POMINO-TROPOMI v1.2.2 tropospheric NO₂ VCDs (sampled based on POMINO-GEMS)

(c)
Y = 1.18 X - 0.16
R = 0.98
NMB = 4.9%
N = 758568
POMINO-GEMS Tropospheric NO₂ VCDs
POMINO-TROPOMI v1.2.2 Tropospheric NO₂ VCDs

(d) POMINO-GEMS tropospheric NO₂ VCDs (sampled based on OMNO2 v4)

(e) OMNO2 v4 tropospheric NO₂ VCDs (sampled based on POMINO-GEMS)

(f)
Y = 0.74 X + 0.16
R = 0.87
NMB = -16.8%
N = 30540
POMINO-GEMS Tropospheric NO₂ VCDs
OMNO2 v4 Tropospheric NO₂ VCDs

(g) POMINO-GEMS tropospheric NO₂ VCDs (sampled based on GOME-2 GDP 4.8)

(h) GOME-2 GDP 4.8 tropospheric NO₂ VCDs (sampled based on POMINO-GEMS)

(i)
Y = 0.69 X + 0.49
R = 0.83
NMB = -1.5%
N = 7515
POMINO-GEMS Tropospheric NO₂ VCDs
GOME-2 GDP 4.8 Tropospheric NO₂ VCDs

$\times 10^{15}$ molec. cm^{-2}

Figure 7. Comparison between POMINO-GEMS and ~~POMINO-TROPOMI tropospheric NO₂ VCDs. Spatial distributions of (a) POMINO-GEMS and (b) POMINO-TROPOMI v1.2.2 tropospheric NO₂ VCDs on a 0.05° × 0.05° grid in JJA 2021. (c) Scatterplot~~**other products** for tropospheric NO₂ VCDs ~~between these two products. Colors represent the data density. Panels~~in JJA 2021. (a-b) Between POMINO-GEMS and **POMINO-TROPOMI v1.2.2 on a 0.05° × 0.05° grid, (d)** ~~and (~~**e)** ~~are absolute~~**between POMINO-GEMS and OMNO2 v4 on a 0.25° × 0.25° grid, and** ~~relative differences~~**(g-h) between POMINO-GEMS and** ~~POMINO-TROPOMI v1.2.2, respectively.~~

~~POMINO-GEMS VCDs are higher than those from POMINO-TROPOMI over eastern China~~**GOME-2 GDP 4.8 on a 0.5° × 0.5° grid. (c), (f)** and ~~smaller over the oceans (Figures 7d and e). These differences are mainly because POMINO-GEMS AMFs are lower (higher) than POMINO-TROPOMI AMFs over polluted~~**(i) are respective scatterplots, in which the colors represent data density. The** ~~regions (ocean). POMINO-GEMS explicitly employs CALIOP-corrected aerosol vertical profiles and re-calculates cloud fraction and cloud pressure based on continuum reflectances and O₂-O₂ SCDs from GEMS~~**in grey mean there are no valid** **observations.** ~~By comparison, POMINO-TROPOMI v1.2.2 does not use CALIOP observations to constrain aerosol vertical profiles; and it takes the FRESCO-wide cloud pressure data from TROPOMI PAL v2.3.1 NO₂ product and re-calculates cloud fraction at 440 nm. Constraint by CALIOP observations results in higher aerosol-concentrated layer heights (Liu et al., 2019), which enhances the "screening" effect on the absorption by NO₂ over polluted regions and leads to lower AMFs. Over remote areas where lightning produced NO₂ is presented at altitudes higher than the aerosol-concentrated layer, higher aerosols tend to enhance the "albedo" effect and lead to higher AMFs (Lin et al., 2015).~~

Figure 7d-f and g-i show the comparison results of POMINO-GEMS tropospheric NO₂ VCDs with

26

566 OMNO2 v4 on a 0.25° × 0.25° grid and GOME-2 GDP 4.8 on a 0.5° × 0.5 °grid averaged over JJA 2021,

567 respectively. POMINO-GEMS NO_2 VCDs exhibit good spatial consistency with the two independent

568 products (R = 0.87 and 0.83), although with slightly lower values than OMNO2 v4 (by 16.8%) and

569 GOME-2 GDP 4.8 (by 1.5%). These VCD differences are expected, considering the differences in the

570 retrieval algorithm. For example, the POMINO-GEMS algorithm implements explicit aerosol

571 corrections in the radiative transfer calculation, while OMNO2 v4 and GOME-2 GDP 4.8 treat aerosols

572 as "effective clouds". POMINO-GEMS accounts for the anisotropy of surface reflectance by adopting

573 MODIS BRDF coefficients, whereas OMNO2 v4 and GOME-2 GDP 4.8 use geometry-dependent and

574 regular LER, respectively. The horizontal resolution of a priori NO_2 profiles in POMINO-GEMS is 25

575 km (and interpolated to 2.5 km), 1° × 1.25 °in OMNO2 v4 and 1.875° × 1.875 °in GOME-2 GDP 4.8

576 (Krotkov et al., 2019; Valks, 2019).

577 Based on comparisons with POMINO-TROPOMI v1.2.2, OMNO2 v4 and GOME-2 GDP 4.8 NO_2

578 VCDs, we conclude that POMINO-GEMS NO_2 columns show good agreement with LEO satellite data,

579 with lower values by 20% at most.

3.3 Validation with MAX-DOAS NO_2 VCD measurements

581 The scatterplot in Figure 8a compares POMINO-GEMS tropospheric NO_2 VCDs in JJA 2021 at all

582 GEMS observation hours with matched ground based MAX-DOAS measurements at nine sites.

583 POMINO-GEMS correlates with MAX-DOAS (R = 0.6266) with a small negative bias (NMB =

584 −15.711.1%). The linear regression shows a slope of 0.4751 and intercept of 3.3734 × 10^{15} molec. cm^{-2},

585 reflecting underestimation of POMINO-GEMS tropospheric NO_2 VCDs on high-NO_2 days.

586
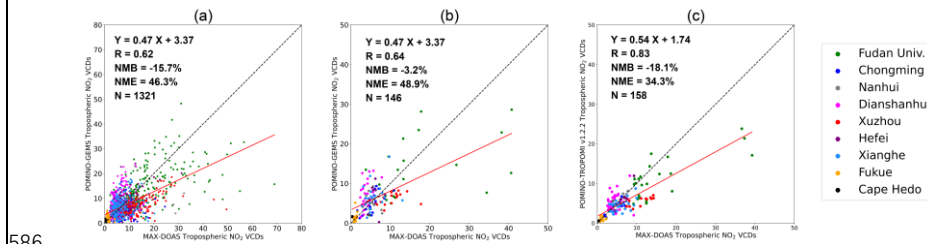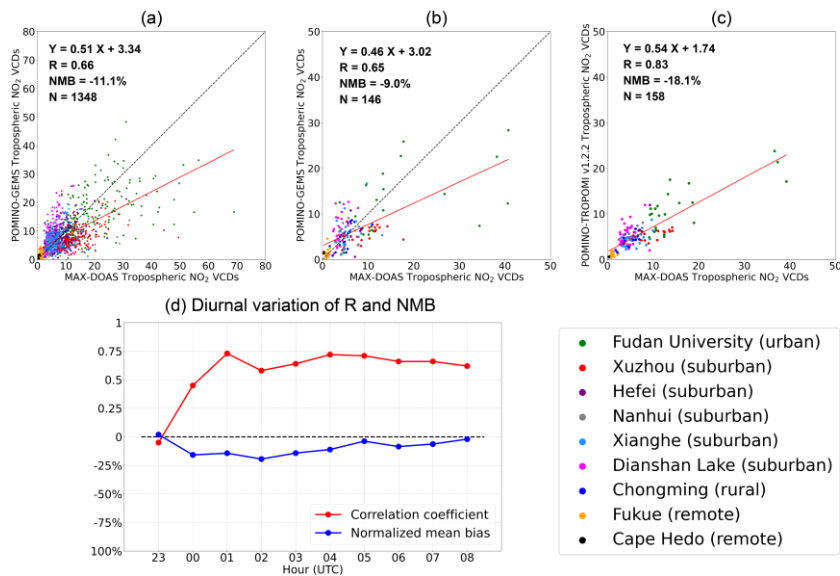
Figure 8. Evaluation of satellite NO$_2$ VCD data using ground-based MAX-DOAS measurements. (a) Scatterplot for tropospheric NO$_2$ VCDs (×10^{15} molec. cm^{-2}) between MAX-DOAS and POMINO-GEMS at all GEMS observation hours in JJA 2021. Each data pair denotes an hour. (b-c) Scatterplots for tropospheric NO$_2$ VCDs (×10^{15} molec. cm^{-2}) in JJA 2021 (b) between MAX-DOAS and POMINO-GEMS at 13:45 – 14:15 LST and (c) between MAX-DOAS and POMINO-TROPOMI v1.2.2. Each data pair denotes a day. Each MAX-DOAS stations are color-coded as indicatedEach MAX-DOAS station is color-coded. (d) Diurnal variations of spatiotemporal correlation coefficients and NMBs of POMINO-GEMS tropospheric NO$_2$ VCDs relative to ground-based MAX-DOAS data.

FiguresFigure 8b-c further use MAX-DOAS measurements to evaluate POMINO-GEMS and POMINO-TROPOMI v1.2.2 tropospheric NO$_2$ VCDs at the overpass time of TROPOMI. In Figure 8b, POMINO-GEMS data at 13:45 – 14:15 LST are used to match the overpass time of TROPOMI. The POMINO-TROPOMI product is evaluated in the context of understanding the relative performance of POMINO-GEMS. Each data point represents a day. FiguresFigure 8b-c showsshow that the day-to-day variability of MAX-DOAS measurements is well captured by POMINO-TROPOMI v1.2.2 (R = 0.83), but less so by POMINO-GEMS (R = 0.6465). Linear regression results show an underestimate of tropospheric NO$_2$ VCDs in POMINO-TROPOMI v1.2.2 product (NMB = −18.1%), as also found in previous studies (Liu et al., 2020). POMINO-GEMS exhibits a small bias (NMB = −3.29.0%), but station-dependent performance is apparent in the scatterplot of Figure 8b. At the two remote sites of Fukue and Cape Hedo with low NO$_2$, POMINO-GEMS tends to overestimateNO$_2$ columns are higher

than those of MAX-DOAS measurements. At the ~~seven urban/suburban~~other sites, the data pairs are more scattered and located both above and below the 1:1 line, resulting in a small NMB. ~~Furthermore, the normalized mean error (NME) of POMINO-GEMS relative to MAX-DOAS measurements (46.3% at all observation hours and 48.9% at 13:45-14:45 LST) is higher than that of POMINO-TROPOMI (34.3%), indicating that the uncertainty in POMINO-GEMS NO$_2$ is larger than POMINO-TROPOMI.~~

Figure 8d shows the NMBs and correlation coefficients of POMINO-GEMS NO$_2$ VCDs relative to ground-based MAX-DOAS data at each hour. The NMBs are negative at most hours except 23:00 UTC (07:00 BJT). The negative NMBs reach a maximum of about 20% at 02:00 UTC (10:00 BJT), and decrease to less than 10% in the afternoon. The correlation coefficients are modest or high (0.45 – 0.73) at most hours, with the exception at the first hour which is likely due to few valid data (N = 17).

Figure 9 ~~also~~ compares the diurnal variation of tropospheric NO$_2$ VCDs between POMINO-GEMS and MAX-DOAS at eight ~~MAX-DOAS~~ stations. At each site, NO$_2$ values are averaged in JJA 2021 at each hour for comparison, and the number of valid days ~~at~~for each hour is also shown ~~in Figure S4~~. The Cape Hedo site is not included because there are few valid MAX-DOAS data points at each hour. ~~Figures 9a-g~~Figure 10a-f show that at the urban and suburban sites, MAX-DOAS NO$_2$ (black lines) peaks in the mid-to-late morning, declines towards the minimum values at noon around 13:00 LST, and then gradually increases in the afternoon. Strong correlation of NO$_2$ diurnal variation between POMINO-GEMS (red solid lines) and MAX-DOAS is found at Xuzhou (R = 0.~~90) and~~82), Hefei (R = 0.~~72), although the correlation is much weaker at~~96), Fudan University (R = 0.~~23) and~~84), Nanhui (R = 0.~~12). At Chongming, 79) and~~ Xianghe ~~and~~ (R = 0.94). At the Dianshan Lake ~~sites~~site, POMINO-GEMS ~~exhibits a maximum in the late afternoon and a second maximum in the mid-morning (Figures 9e-g), a pattern which is poorly correlated with~~NO$_2$ columns increase but MAX-DOAS ~~(R = −0.02, −0.23 and −0.66, respectively). At~~ data decrease from 08:00 to 09:00 LST, resulting in a lower correlation coefficient (R = 0.60). At Chongming and Fukue sites, MAX-DOAS NO$_2$ shows a peak in the morning ~~and then declines to low values around 1 × 10^{15} molec. cm^{-2}~~without evident increase in the early afternoon, but this diurnal pattern is not fully captured by POMINO-GEMS. ~~Overall, the mixed performance at these eight sites suggests that more work is warranted to further improve the~~At Fukue, POMINO-GEMS ~~retrieval algorithm.~~NO$_2$ exhibit abrupt changes at 12:00 and 13:00 LST due to few valid data.

635
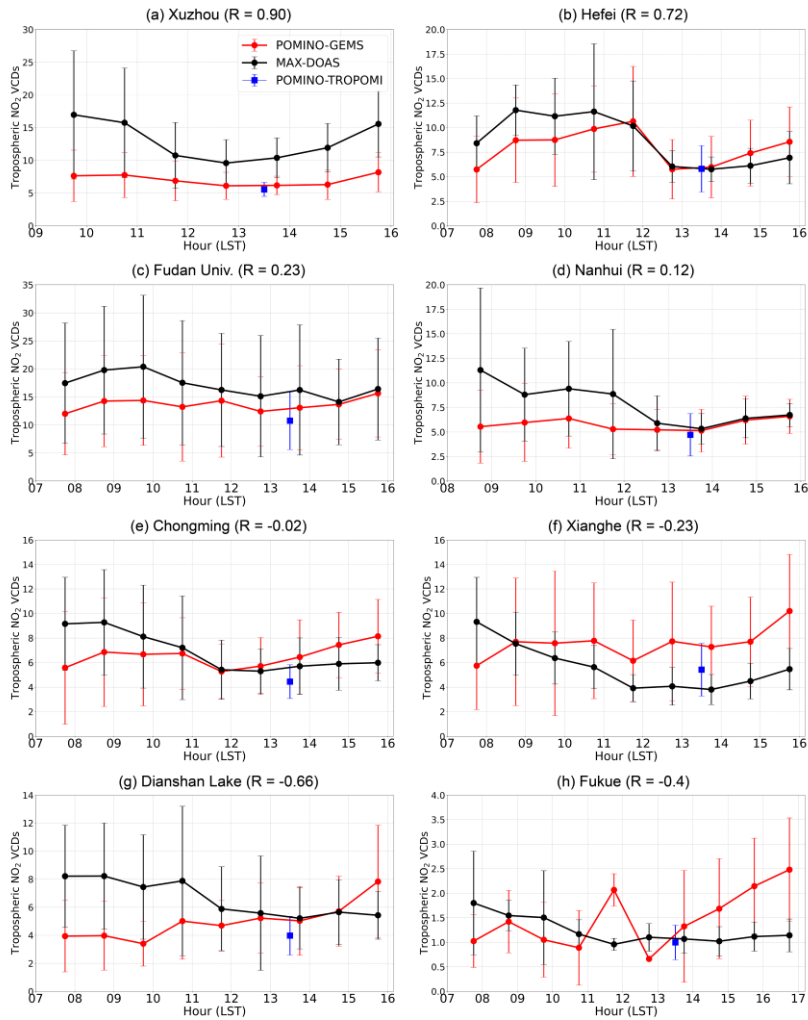
In addition, comparison of POMINO-GEMS diurnal variation with NO$_2$ data from GOME-2 in the
636 morning and OMI and TROPOMI in the early afternoon shows good agreement at Hefei, Nanhui,
637 Dianshan Lake, Chongming and Fukue sites. The differences between POMINO-GEMS to MAX-DOAS
638 NO$_2$ VCDs are comparable or smaller than those between LEO satellite and MAX-DOAS NO$_2$ VCDs.
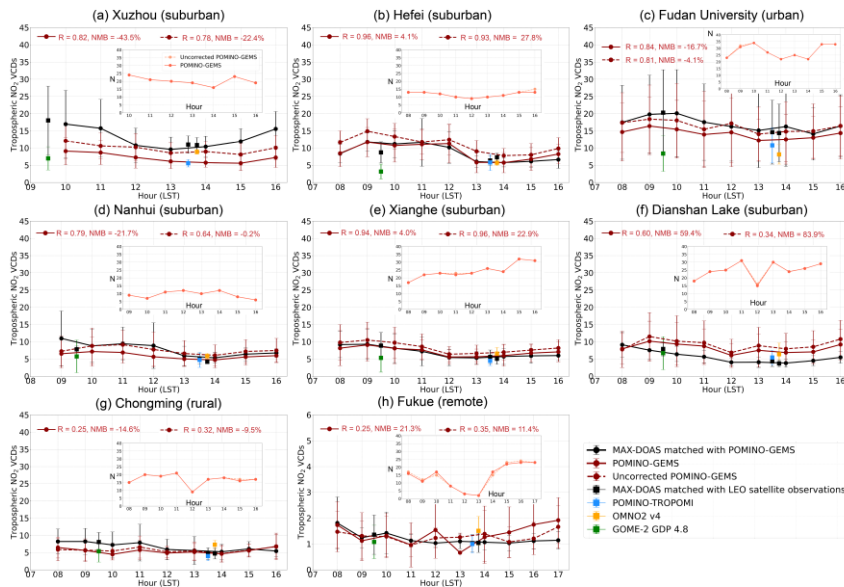
Figure 9. Diurnal variation of hourly tropospheric NO₂ VCDs (× 10¹⁵ molec. cm⁻²) ~~from~~of MAX-DOAS (black lines), and POMINO-GEMS with TROPOMI correction (red solid lines). and re-calculated POMINO-GEMS without TROPOMI correction (red dashed lines) at eight sites in JJA 2021. The error bars denote the standard deviation of MAX-DOAS and POMINO-GEMS NO₂ at each hour ~~in JJA 2021~~, respectively. ~~The temporal~~Diurnal correlation ~~coefficients~~and all-hour-mean NMB of POMINO-GEMS against MAX-DOAS data are ~~also~~ shown. ~~In~~ The number of valid days for each ~~panel, the blue square~~hour is also presented. The black squares with an error bar ~~represents~~represent the mean value and standard deviation of MAX-DOAS tropospheric NO₂ VCDs matched with POMINO-TROPOMI v1.2.2 ~~NO₂ in JJA 2021~~(blue squares), OMNO2 v4 (orange squares) and GOME-2 GDP 4.8 (green squares), respectively.

As we use TROPOMI total NO₂ SCDs to correct those of GEMS, this may influence the NO₂ diurnal variation of original GEMS observations. Thus we also compare MAX-DOAS data with re-calculated POMINO-GEMS tropospheric NO₂ VCDs without correction in total SCDs (red dashed lines in Figure 9). Compared to our default POMINO-GEMS data (with correction), excluding the correction leads to lower diurnal correlation coefficients at Xuzhou, Hefei, Fudan University, Nanhui and Dianshan Lake, but higher correlation coefficients at Xianghe, Chongming and Fukue. Excluding the correction increases the NMB at three sites but decreases the NMB at five sites. We conclude that at these eight sites (in the eastern areas), no significant influence on the diurnal variation of POMINO-GEMS tropospheric NO₂ VCDs is brought in through TROPOMI-based correction for total NO₂ SCDs.

Figure 10 compares the diurnal variations between POMINO-GEMS and mobile-car MAX-DOAS

31

tropospheric NO_2 VCD data in the Three Rivers' Source region on the Tibetan Plateau. Results of POMINO-GEMS with and without total SCD correction are shown in the red solid and dashed lines, respectively. Mobile-car MAX-DOAS data show an evident decrease of tropospheric NO_2 VCDs from the morning to noon with little change thereafter. Such NO_2 diurnal patterns reflect the spatial and temporal variations of tropospheric NO_2 along the driving route. The high NO_2 values with large standard deviation at 09:00 BJT is due to enhanced pollution and variability in the morning when the car is in or near the Xining city. The NO_2 diurnal variations of POMINO-GEMS with correction correlate well with those of mobile-car MAX-DOAS data ($R = 0.81$). In contrast, POMINO-GEMS without total SCD correction exhibits much poorer correlation with mobile-car MAX-DOAS data, due to the erroneous increase in the afternoon.

Overall, the validation results with independent ground-based and mobile-car MAX-DOAS measurements provide confidence on the general characteristics of POMINO-GEMS NO_2 diurnal variations.
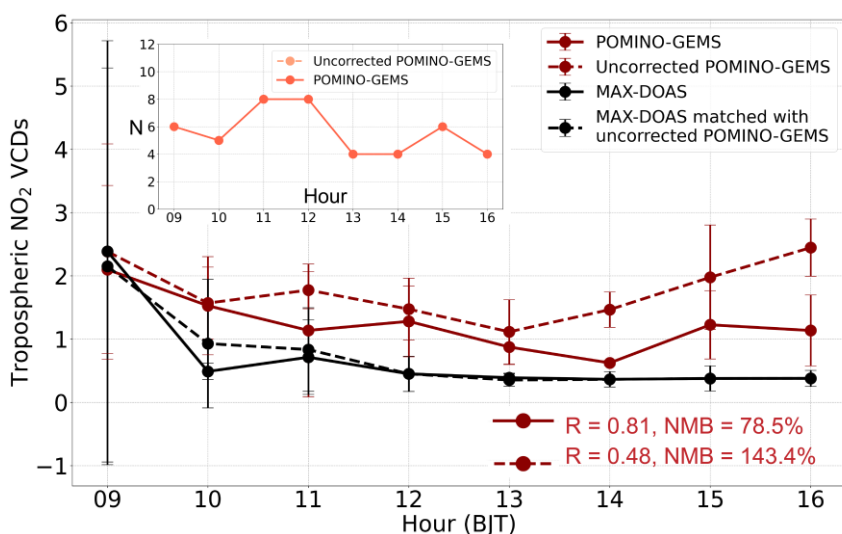
Figure 10. Diurnal variation of hourly mean tropospheric NO_2 VCDs ($\times 10^{15}$ molec. cm^{-2}) of mobile-car MAX-DOAS and POMINO-GEMS in the Three Rivers' Source region. The black solid lines denote MAX-DOAS data that spatiotemporally match with POMINO-GEMS with total SCD correction (red solid lines). The black dashed lines denote MAX-DOAS data that spatiotemporally match with POMINO-GEMS without correction (red dashed lines). The error bars denote the standard deviation of MAX-DOAS and POMINO-GEMS NO_2 at each hour during the field campaign, respectively. Values for diurnal correlation and mean NMB of POMINO-GEMS relative to MAX-DOAS are shown. The number of days with valid data for each hour is also presented.

3.4 Validation with surface NO$_2$ concentration measurements from MEE

The scatterplot in Figure ~~10a further~~11a compares surface NO$_2$ concentrations derived from POMINO-GEMS with MEE measurements at all hours. ~~Here, each data pair represents a site and hour averaged over all days in JJA 2021.~~ POMINO-GEMS derived surface NO$_2$ concentrations show good agreement with MEE measurements in terms of spatiotemporal correlation ($R = 0.$~~76~~78) and bias (NMB = ~~−24.1%). Despite the overall underestimate, POMINO-GEMS derived surface NO$_2$ concentrations show overestimation~~26.3%), but are higher than those of MEE at some high-value situations, which mainly occur over the YRD region (Figure ~~S5~~S14). These differences reflect errors in POMINO-GEMS NO$_2$ VCDs, in the conversion from tropospheric VCDs to surface concentrations, and~~/or in MEE measurements. In particular, the MEE measurements are contaminated by oxidation products of NO$_2$ (e.g., HNO$_3$ and PANs) and tend~~ in MEE data (due to ~~overestimate the actual concentrations of NO$_2$ (Liu et al., 2018), with the extent of~~ potential contamination ~~more severe for more aged air.~~by nitric acid and organic nitrates (Liu et al., 2018a)).

(d) Diurnal variation of R and NMB
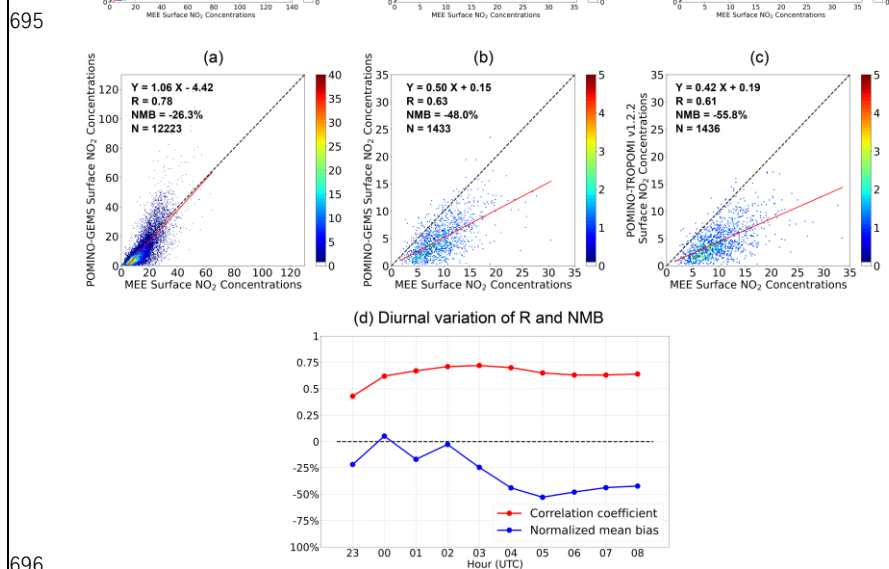
Figure ~~10~~11. Evaluation of satellite-derived surface NO$_2$ concentrations (μg m^{-3}) using MEE measurements in JJA 2021. (a) Scatterplot for ~~surface NO$_2$ concentrations (μg m^{-3}) between~~ MEE and POMINO-GEMS at all GEMS observation hours averaged over all days in JJA 2021. (b-~~c~~) Scatterplot for ~~surface NO$_2$ concentrations in JJA 2021 (b) between~~ MEE and POMINO-GEMS at 13:45 – 14:15 LST~~, and~~. (c) ~~between~~Scatterplot for MEE and POMINO-TROPOMI v1.2.2. The color bar represents the data density. (d) Diurnal variations of spatiotemporal correlation coefficients and NMBs of POMINO-GEMS derived surface NO$_2$ concentrations relative to MEE measurements.

~~Figures 10b~~Figure 11b-c show validation results for satellite-derived surface NO$_2$ concentrations with MEE measurements at ~~855 sites at~~ the overpass time of TROPOMI (i.e., early afternoon). Here, each data pair denotes a MEE site. POMINO-GEMS results at 13:45–~~~~14:15 LST are used to match the overpass time of TROPOMI data. Overall, both satellite-based datasets show good spatial correlation with MEE measurements~~, with correlation coefficients of~~ (R = 0.~~55~~63 and 0.~~57, respectively.~~61). POMINO-GEMS exhibits higher linear regression slope (0.~~44~~50) with smaller NMB (−~~37.2%)~~ and ~~NME (40.6~~48.0%). The values of satellite data are lower than those from MEE ~~measurements,~~, especially in the afternoon (Figure 11d). This is in part because of the aforementioned contamination issues in MEE data, which becomes severer in the afternoon as the air gets more aged throughout the daytime.

Figure ~~11 further~~12a examines the diurnal variation of surface NO$_2$ concentrations averaged over JJA 2021 ~~and~~at all sites. The MEE data show a smooth and monotonic decline from the early morning to the early afternoon, with a slight increase beginning at 15:00 LST. This diurnal pattern differs from those seen in ground-based MAX-DOAS VCD data (Figure 9), due to the difference in sampling size between MEE and MAX-DOAS, ~~as well as~~ the diurnal variation of NO$_2$ vertical distribution ~~of NO$_2$~~that affects the relationship between surface and columnar NO$_2$~~,~~, as well as the insensitivity of NO$_2$ columns to changes in PBL heights. POMINO-GEMS derived surface NO$_2$ concentrations show similar diurnal variations to those ~~from~~of MEE (R = 0.~~95~~97), although with a peak at 10:00 LST and a gradual increase beginning at 14:00 LST. The discrepancies between POMINO-GEMS and MEE surface NO$_2$ concentrations at different hours are likely caused by the assumed constant correction factor of 2 to account for the vertical gradient of NO$_2$ from the height of ground instrument to the center of the first model layer (Section 2.2). In the morning when the PBL is low, most NO$_2$ molecules are near the ground and the vertical gradient of NO$_2$ over polluted regions is the largest in the daytime, so the factor of 2 may lead to underestimation of derived surface NO$_2$ concentrations. In contrast, in the afternoon, the PBL mixing is much stronger and the vertical gradient of NO$_2$ is much smaller, thus the factor of 2 may lead

728   to overestimated surface NO$_2$ concentrations. Note that the consistency between POMINO-GEMS and

729   MEE data does not depend on the total SCD correction (Table S4).

730
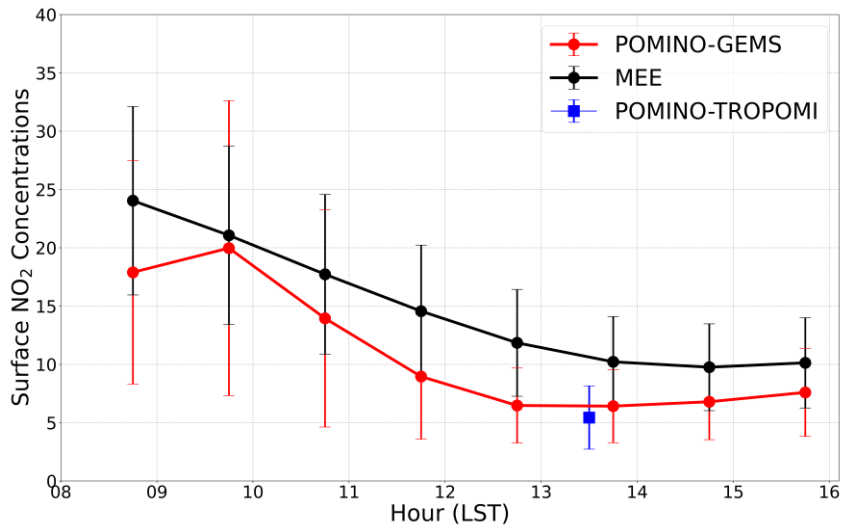
731   ~~Figure 11.~~To quantify the influences of the diurnal variation of hourly column-to-surface ratio from

732   GEOS-Chem simulations, we compare the MEE measurements with POMINO-GEMS derived surface

733   NO$_2$ concentrations using daily column-to-surface ratio (Figure S15). As expected, POMINO-GEMS

734   derived NO$_2$ concentrations show a similar diurnal variation as the tropospheric NO$_2$ VCDs do, with two

735   peaks in the mid-morning and afternoon, and a minimum at noon. The temporal correlation coefficient

736   with MEE is only about 0.23. Thus it is more reasonable to use hourly ratio for comparison with MEE

737   measurements, as done in our study.

738   To further test the reliability of our VCD-to-surface-concentration conversion method (Eq. (9)), we

739   apply the same method to MAX-DOAS NO$_2$ VCDs and compare the resulting surface NO$_2$

740   concentrations with MEE data. As shown in Figure S16, the diurnal variation of MAX-DOAS derived

741   surface NO$_2$ concentrations correlates well with that of MEE measurements ($R = 0.96$), in support of our

742   conversion method.
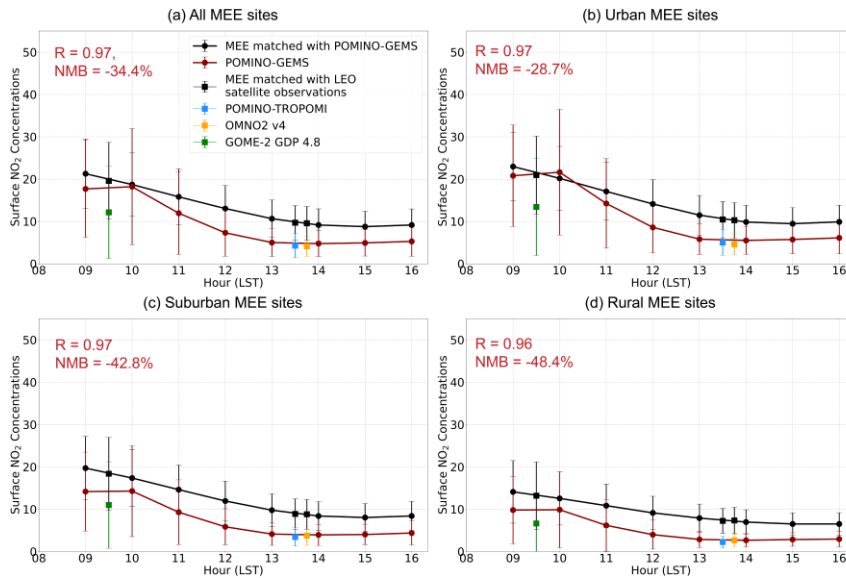
Figure 12. Diurnal variation of hourly surface NO₂ concentrations (μg m⁻³) ~~for~~of MEE **(back lines)** and POMINO-GEMS **(red lines)** in JJA 2021. **(a) At all MEE sites, (b) at urban sites, (c) at suburban sites and (d) at rural sites.** The error bars denote the standard deviation of MEE and POMINO-GEMS derived surface NO₂ concentrations at each hour in JJA 2021, respectively. **Diurnal correlation and mean NMB of POMINO-GEMS relative to MEE are also listed.** The ~~blue square~~**black squares** with an error bar ~~represents~~**represent** the mean value and standard deviation of **MEE data matched with** POMINO-TROPOMI v1.2.2 ~~derived surface NO₂ concentrations~~**(blue squares), OMNO2 v4 (orange squares) and GOME-2 GDP 4.8 (green squares), respectively.**

Figure 12b-d show the comparison of NO₂ diurnal variations for different groups of MEE sites. The diurnal variations of POMINO-GEMS derived surface NO₂ concentrations show similar characteristics over urban, suburban and rural regions, and all correlate well with those of MEE data. Meanwhile, surface NO₂ concentrations derived from LEO satellite observations also agree well with those of POMINO-GEMS, except that POMINO-GEMS derived surface NO₂ concentrations are higher than those of GOME-2 GDP 4.8 by about 40% – 60%. We conclude that validation with extensive MEE measurements presents promising performance of POMINO-GEMS retrievals, especially the great agreement of POMINO-GEMS NO₂ diurnal variation with MEE data over urban, suburban and rural regions.

3.5 Error estimates for POMINO-GEMS tropospheric NO₂ VCDs

Total retrieval errors for POMINO-GEMS tropospheric NO₂ VCDs are ~~compounded~~derived from

36

763 the calculations of total SCDs, stratospheric SCDs, and tropospheric AMFs. Spatial and temporal

764 averaging across GEMS pixels can greatly reduce the random errors, but will not affect the systematic

765 errors. Here, we provide a preliminary estimate of POMINO-GEMS errors for the summertime retrieval

766 ~~errors~~discussed above.

767   As described in Section 2, we calculate hourly total SCDs based on the original GEMS SCD data

768 and daily TROPOMI-guided corrections. ~~We tentatively estimate the error in our corrected total SCD~~

769 ~~data to be 10%, which is the same as the TROPOMI total SCD error (Van Geffen et al., 2022a),~~

770 ~~considering that we essentially adjust GEMS total SCDs to match TROPOMI values. In constructing the~~

771 ~~stratospheric NO$_2$ SCDs, the stratospheric VCDs are taken from TROPOMI PAL v2.3.1, scaled based on~~

772 ~~GEOS-Chem simulations to account for diurnal variation, and then applied with geometric AMFs. We~~

773 ~~assign an error of 0.2 × 10^{15} molec. cm^{-2} (5% 10%) to our hourly stratospheric SCDs, the same as the~~

774 ~~value for TROPOMI~~According to the GEMS ATBD of NO$_2$ retrieval algorithm, the SCD errors from the

775 DOAS method are < 5.65% at high-NO$_2$ conditions (NO$_2$ VCD > 1 × 10^{15} molec. cm^{-2}) (Lee et al., 2020).

776 The NO$_2$ SCD errors of TROPOMI are reported to be 0.5 – 0.6 × 10^{15} molec. cm^{-2} (10% in a relative

777 sense) (Van Geffen et al., 2022a). ~~As such,~~Given the assumption we ~~assume no~~made in adjusting GEMS

778 total SCDs to match TROPOMI values, we tentatively estimate the error ~~contributions~~in our corrected

779 total SCD data to be 0.5 – 0.7 × 10^{15} molec. cm^{-2} (10% in a relative sense) for most regions and 0.9 ×

780 10^{15} molec. cm^{-2} (20% – 30%) at the edge of the northwestern GEMS FOV.

781   In constructing the stratospheric NO$_2$ SCDs, the stratospheric VCDs are taken from ~~the GEOS-~~

782 ~~Chem~~TROPOMI PAL v2.3.1, scaled based ~~scaling and~~ on GEOS-CF v1 stratospheric NO$_2$ to account

783 for diurnal variation, and then applied with geometric AMFs. We assign a constant error of 0.2 × 10^{15}

784 molec. cm^{-2} (5% – 10%) to our hourly stratospheric SCDs, the same as the value for TROPOMI (Van

785 Geffen et al., 2022a). Few studies have assessed the accuracy of stratospheric NO$_2$ and its diurnal

786 variation from GEOS-CF data (Knowland et al., 2022b), but our comparison between GEOS-CF and

787 TROPOMI shows great consistency (Section 2.1.5). As most of the errors in total SCDs are absorbed in

788 the ~~calculation of stratospheric SCDs~~stratosphere-troposphere separation step (Van Geffen et al., 2015),

789 the errors in tropospheric SCDs should be ~~0.2 × 10^{15} molec. cm^{-2} (5% 40%) at most~~10% – 30%

790 depending on different cases, with higher relative biases in cleaner situations.

791   Tropospheric AMF calculations are the dominant error source for retrieved tropospheric NO$_2$ VCDs

792 over polluted regions. According to Liu et al. (2020)~~, the AMF errors caused by uncertainties in surface~~

793 ~~reflectance and a priori NO₂ profiles are about 10% each, and errors induced by uncertainties in aerosol~~

794 ~~parameters are about 10% in clean regions and 20% for heavily polluted situations. We further assume~~

795 ~~that the O₂-O₂ cloud retrieval algorithm introduces another error at the 10% level to the NO₂ AMFs. The~~

796 ~~overall AMF errors for POMINO-GEMS are estimated to be 20%–30%, as determined by adding these~~

797 ~~errors in quadrature.~~

798 , the AMF errors caused by uncertainty in surface reflectance are about 10%, and errors induced by

799 uncertainties in aerosol parameters are about 10% in clean regions and 20% for heavily polluted

800 situations. We further assume that the O_2-O_2 cloud retrieval algorithm introduces another error at the 10%

801 level to the NO_2 AMFs. The uncertainty in a priori NO_2 vertical profiles is estimated to cause an AMF

802 error by 10% (Liu et al., 2020). Yang et al. (2023) suggested that the NO_2 profiles from GEOS-Chem

803 (version 13.3.4) might contain incorrect timing of PBL mixing growth in the morning and thus introduce

804 a relative root-mean-square error of 7.6% and NMB of 2.7% in AMF; however, this error could be greatly

805 dampened by averaging over a long time period. The free tropospheric NO_2 bias in GEOS-Chem NO_2

806 profiles might also contribute to the retrieval errors especially over remote regions. Adding these errors

807 in quadrature leads to the overall AMF errors for POMINO-GEMS at 20% – 40%.

808 The overall uncertainty in POMINO-GEMS tropospheric NO_2 VCDs is estimated by adding in

809 quadrature the errors in tropospheric NO_2 SCDs and AMFs, when these errors are expressed in the

810 relative sense. For ~~pixels over~~ remote regions with low tropospheric NO_2 abundances, the overall

811 retrieval ~~uncertainty is~~uncertainties can reach 30% – 50% and are dominated by errors in tropospheric

812 SCDs ~~and can reach 0.2 × 10¹⁵ molec. cm⁻² (or 30%–50%).~~. For ~~pixels~~regions with abundant tropospheric

813 NO_2, the ~~uncertainty~~uncertainties of retrieved tropospheric VCDs ~~is~~are dominated by the AMF errors

814 and ~~is~~are estimated to be about ~~25%–35%. The~~20% – 30%.

815 As shown in Figure 8d and Figure 11d, the maximum negative NMB of POMINO-GEMS

816 tropospheric NO_2 VCDs relative to ground-based MAX-DOAS data is about 20% in the mid-morning,

817 and the NMB of POMINO-GEMS derived surface NO_2 concentrations to MEE measurements is −30%

818 on average. Thus our estimated error magnitude is supported by the ~~NMB and NME values shown in the~~

819 ~~validation results against~~independent ground-based MAX-DOAS and MEE data ~~(Figure 8a, b and Figure~~

820 ~~10a, b).~~.

4. Conclusions

The GEMS instrument provides an unprecedented opportunity for air quality monitoring at a high spatiotemporal resolution. Our POMINO-GEMS algorithm retrieves tropospheric NO_2 VCDs as a research product. The algorithm first calculates hourly tropospheric NO_2 SCDs through fusion of total NO_2 SCDs from the GEMS v1.0 L2 NO_2 product, total and stratospheric NO_2 columns from the TROPOMI PAL v2.3.1 L2 NO_2 product, and stratospheric NO_2 diurnal variations from the GEOS-~~Chem simulations~~CF v1 dataset. The fusion approach reduces the high bias in total SCDs and removes the stripe-like patterns in the official GEMS v1.0 product. Our algorithm then calculates tropospheric NO_2 AMFs to convert SCDs to VCDs. A preliminary estimate of retrieval errors is also given.

Our initial POMINO-GEMS data for JJA 2021 shows high values of tropospheric NO_2 VCDs with clear hotspots ($> 10 \times 10^{15}$ molec. cm^{-2}) over regions where anthropogenic emissions of NO_x are abundant. The spatial gradients of tropospheric NO_2 VCDs from urban centers to surrounding areas are substantial in the morning due to traffic emissions, ~~and~~but the gradients are much reduced at noon and in the afternoon. ~~By comparison, a roughly monotonic~~A gradual increase of tropospheric NO_2 VCDs from the morning to ~~the afternoon~~ noon is observed over clean regions of western China, likely as a result of enhanced biogenic emissions. Over high NO_2 regions where anthropogenic activities dominate the NO_x emissions, NO_2 columns increase until a peak at 09:00 – 10:00 LST, decrease to the minimum at noon and then increase in the afternoon again. Such characteristics of NO_2 diurnal variations are associated with the changes in natural and anthropogenic NO_x emissions, photochemistry and atmospheric transport.

POMINO-GEMS tropospheric NO_2 VCDs agree well with POMINO-TROPOMI v1.2.2 in terms of spatial correlation (0.~~97~~98) and NMB (~~3.6~~4.9%). POMINO-GEMS ~~is also~~data are also consistent with the OMNO2 v4 tropospheric NO_2 VCD product in the early afternoon and GOME-2 GDP 4.8 tropospheric NO_2 VCD product in the morning, with R of 0.87 and 0.83, and NMB of −16.8% and −1.5%, respectively.

POMINO-GEMS tropospheric NO_2 VCDs are comparable with ground-based MAX-DOAS measurements at nine ~~rural/suburban/urban~~ground-based sites with a small NMB (~~−15.7~~11.1%), although the ~~correlations are~~correlation is modest ($R = 0.~~62~~66$). Both the bias and correlation values are smaller than POMINO-TROPOMI v1.2.2 (NMB = −18.1%, $R = 0.83$). More importantly, POMINO-GEMS well captures the diurnal variation of MAX-DOAS NO_2 VCDs at ~~the~~ Xuzhou ($R = 0.~~90) and~~82$), Hefei ($R = 0.~~72~~96$), Fudan University ($R = 0.84$), Nanhui ($R = 0.79$), Xianghe ($R = 0.94$) and Dianshan

39

851 Lake ($R = 0.60$) sites ~~but not~~, although the correlations are relatively poor at ~~others, for reasons that are~~

852 ~~not clear at present.~~Chongming and Fukue sites. Comparison with mobile-car MAX-DOAS

853 measurements in the Three Rivers' Source region on the Tibetan Plateau also shows good correlation in

854 NO_2 diurnal variation ($R = 0.81$).

855   We also compare surface NO_2 concentrations derived from tropospheric NO_2 VCDs ~~from~~in

856 POMINO-GEMS and POMINO-TROPOMI v1.2.2 ~~products~~ against MEE ~~measurements~~data, taking

857 advantage of the large number of MEE sites. ~~For 855 selected sites at all GEMS observation hours,~~

858 POMINO-GEMS derived surface NO_2 concentration data exhibit a small NMB (−~~24.1~~26.3%). For these

859 sites at TROPOMI overpass times, POMINO-GEMS derived surface NO_2 concentrations show a smaller

860 magnitude of NMB (−~~37.2~~48.0%) than POMINO-TROPOMI v1.2.2 (−~~47.0~~55.8%). Excellent agreement

861 in diurnal variation between POMINO-GEMS derived and MEE NO_2 ~~averaged over all sites~~ is exhibited

862 over all ($R = 0.$~~95)~~97), urban ($R = 0.97$), suburban ($R = 0.97$) and rural ($R = 0.96$) sites.

863   Overall, our comprehensive validation process highlights the good performance of POMINO-

864 GEMS tropospheric NO_2 VCD product, both in magnitude and spatiotemporal variation. However, there

865 are still several limitations in our study. To address the systematic overestimation and stripes problems

866 in the original GEMS data, we correct GEMS total NO_2 SCDs by using TROPOMI data as a temporary

867 solution. For example, we implement a simple geometric correction to combine GEMS and TROPOMI

868 total NO_2 SCDs, but their differences in scattering geometry are only partly accounted for. Thus this

869 correction works well in most regions, but may introduce SCD uncertainties up to 0.9×10^{15} molec. cm⁻

870 ² (20% − 30%) at the edge of the northwestern GEMS FOV. Currently, the Environmental Satellite Center

871 of South Korea is updating the NO_2 SCD data to v2.0. We will update our POMINO-GEMS algorithm

872 accordingly, once the updated official NO_2 product becomes available to provide ~~the~~ necessary inputs

873 for our research product. In addition, in the conversion from NO_2 VCDs to surface concentrations, we

874 use a constant correction factor of 2 to account for the strong NO_2 vertical gradient near the surface. This

875 simple treatment does not account for the diurnal variation of the correction factor, and thus may

876 introduce errors in the derived surface NO_2 concentrations. Nevertheless, the current POMINO-GEMS

877 data serve as our initial attempt to derive the diurnal variations of tropospheric NO_2 at a high

878 spatiotemporal resolution from GEMS, and they are expected to offer a useful source of information for

879 various applications such as air quality analysis and emission constraint.

880

890

897

899

903

References

905   Beirle, S., Boersma, K. F., Platt, U., Lawrence, M. G., and Wagner, T.: Megacity Emissions and

906   Lifetimes of Nitrogen Oxides Probed from Space, Science, 333, 1737-1739, 10.1126/science.1207824,

907   2011.

908   Biswas, M. S. and Mahajan, A. S.: Year-long Concurrent MAX-DOAS Observations of Nitrogen

41

Dioxide and Formaldehyde at Pune: Understanding Diurnal and Seasonal Variation Drivers, Aerosol and Air Quality Research, 21, 200524, 10.4209/aaqr.200524, 2021.

Boersma, K. F., Eskes, H. J., and Brinksma, E. J.: Error analysis for tropospheric NO2 retrieval from space, Journal of Geophysical Research: Atmospheres, 109, n/a-n/a, 10.1029/2003jd003962, 2004.

Boersma, K. F., Jacob, D. J., Eskes, H. J., Pinder, R. W., Wang, J., and Van Der A, R. J.: Intercomparison of SCIAMACHY and OMI tropospheric NO$_2$ columns: Observing the diurnal evolution of chemistry and emissions from space, Journal of Geophysical Research, 113, 10.1029/2007jd008816, 2008.

Boersma, K. F., Jacob, D. J., Trainic, M., Rudich, Y., Desmedt, I., Dirksen, R., and Eskes, H. J.: Validation of urban NO$_2$ concentrations and their diurnal and seasonal variations observed from the SCIAMACHY and OMI sensors using in situ surface measurements in Israeli cities, Atmospheric Chemistry and Physics, 9, 3867-3879, 10.5194/acp-9-3867-2009, 2009.

Boersma, K. F., Eskes, H. J., Dirksen, R. J., van der A, R. J., Veefkind, J. P., Stammes, P., Huijnen, V., Kleipool, Q. L., Sneep, M., Claas, J., Leitão, J., Richter, A., Zhou, Y., and Brunner, D.: An improved tropospheric NO2 column retrieval algorithm for the Ozone Monitoring Instrument, Atmospheric Measurement Techniques, 4, 1905-1928, 10.5194/amt-4-1905-2011, 2011.

Burrows, J. P.: The Global Ozone Monitoring Experiment (GOME) : Mission concept and first scientific results, Journal of Atmospheric Sciences, 56, 2340-2352, 1999.

Callies, J., Corpaccioli, E., Eisinger, M., Hahne, A., and Lefebvre, A.: GOME-2 – Metop's Second-Generation Sensor for Operational Ozone Monitoring,

Chen, L., Lin, J., Martin, R., Du, M., Weng, H., Kong, H., Ni, R., Meng, J., Zhang, Y., Zhang, L., and van Donkelaar, A.: Inequality in historical transboundary anthropogenic PM2.5 health impacts, Science Bulletin, https://doi.org/10.1016/j.scib.2021.11.007, 2021.

Chen, L., Lin, J., Ni, R., Kong, H., Du, M., Yan, Y., Liu, M., Wang, J., Weng, H., Zhao, Y., Li, C., and Martin, R. V.: Historical transboundary ozone health impact linked to affluence, Environmental Research Letters, 17, 104014, 10.1088/1748-9326/ac9009, 2022.

Cheng, S., Cheng, X., Ma, J., Xu, X., Zhang, W., Lv, J., Bai, G., Chen, B., Ma, S., Ziegler, S., Donner, S., and Wagner, T.: Mobile MAX-DOAS observations of tropospheric NO2 and HCHO during summer over the Three Rivers' Source region in China, Atmos. Chem. Phys., 23, 3655-3677,

10.5194/acp-23-3655-2023, 2023.

Cooper, M. J., Martin, R. V., Hammer, M. S., Levelt, P. F., Veefkind, P., Lamsal, L. N., Krotkov, N. A., Brook, J. R., and Mclinden, C. A.: Global fine-scale changes in ambient NO2 during COVID-19 lockdowns, Nature, 601, 380-387, 10.1038/s41586-021-04229-0, 2022.

Crutzen, P. J.: The influence of nitrogen oxides on the atmospheric ozone content, Quarterly Journal of the Royal Meteorological Society, 96, 320-325, 10.1002/qj.49709640815, 1970.

Cui, Y., Lin, J., Song, C., Liu, M., Yan, Y., Xu, Y., and Huang, B.: Rapid growth in nitrogen dioxide pollution over Western China, 2005–2013, Atmos. Chem. Phys., 16, 6207-6221, 10.5194/acp-16-6207-2016, 2016.

Dirksen, R. J., Boersma, K. F., Eskes, H. J., Ionov, D. V., Bucsela, E. J., Levelt, P. F., and Kelder, H. M.: Evaluation of stratospheric NO2retrieved from the Ozone Monitoring Instrument: Intercomparison, diurnal cycle, and trending, Journal of Geophysical Research, 116, 10.1029/2010jd014943, 2011.

Eastham, S. D., Weisenstein, D. K., and Barrett, S. R. H.: Development and evaluation of the unified tropospheric–stratospheric chemistry extension (UCX) for the global chemistry-transport model GEOS-Chem, Atmospheric Environment, 89, 52-63, https://doi.org/10.1016/j.atmosenv.2014.02.001, 2014.

Eskes, H., Van Geffen, J., Sneep, M., Veefkind, P., Niemeier, S., and Zehner, C.: S5P Nitrogen Dioxide v02.03.01 intermediate reproecessing on the S5P-PAL system: Readme file, 2021.

Ghude, S. D., Karumuri, R. K., Jena, C., Kulkarni, R., Pfister, G. G., Sajjan, V. S., Pithani, P., Debnath, S., Kumar, R., Upendra, B., Kulkarni, S. H., Lal, D. M., Vander A, R. J., and Mahajan, A. S.: What is driving the diurnal variation in tropospheric NO2 columns over a cluster of high emission thermal power plants in India?, Atmospheric Environment: X, 5, 100058, https://doi.org/10.1016/j.aeaoa.2019.100058, 2020.

Grubbs, F. E.: Sample Criteria for Testing Outlying Observations, The Annals of Mathematical Statistics, 21, 27-58, 10.1214/aoms/1177729885, 1950.

Gu, D., Wang, Y., Smeltzer, C., and Boersma, K. F.: Anthropogenic emissions of NOxover China: Reconciling the difference of inverse modeling results using GOME-2 and OMI measurements, Journal of Geophysical Research: Atmospheres, 119, 7732-7740, 10.1002/2014jd021644, 2014.

Hendrick, F., Müller, J.-F., Clémer, K., Wang, P., De Mazière, M., Fayt, C., Gielen, C., Hermans, C., Ma, J. Z., Pinardi, G., Stavrakou, T., Vlemmix, T., and Van Roozendael, M.: Four years of ground-based

MAX-DOAS observations of HONO and NO_2 in the Beijing area, Atmospheric Chemistry and Physics, 14, 765-781, 10.5194/acp-14-765-2014, 2014.

Herman, J., Abuhassan, N., Kim, J., Kim, J., Dubey, M., Raponi, M., and Tzortziou, M.: Underestimation of column NO2 amounts from the OMI satellite compared to diurnally varying ground-based retrievals from multiple PANDORA spectrometer instruments, Atmos. Meas. Tech., 12, 5593-5612, 10.5194/amt-12-5593-2019, 2019.

Hoek, G., Krishnan, R. M., Beelen, R., Peters, A., Ostro, B., Brunekreef, B., and Kaufman, J. D.: Long-term air pollution exposure and cardio- respiratory mortality: a review, Environmental Health, 12, 43, 10.1186/1476-069X-12-43, 2013.

Jing, B., Wu, L., Mao, H., Gong, S., He, J., Zou, C., Song, G., Li, X., and Wu, Z.: Development of a vehicle emission inventory with high temporal–spatial   resolution based on NRT traffic data and its impact on air pollution in   Beijing – Part 1: Development and evaluation of vehicle emission inventory, Atmospheric Chemistry and Physics, 16, 3161-3170, 10.5194/acp-16-3161-2016, 2016.

Kanaya, Y., Irie, H., Takashima, H., Iwabuchi, H., Akimoto, H., Sudo, K., Gu, M., Chong, J., Kim, Y. J., Lee, H., Li, A., Si, F., Xu, J., Xie, P.-H., Liu, W.-Q., Dzhola, A., Postylyakov, O., Ivanov, V., Grechko, E., Terpugova, S., and Panchenko, M.: Long-term MAX-DOAS network observations of NO_2 in Russia and Asia (MADRAS) during the period 2007–2012: instrumentation, elucidation of climatology, and comparisons with OMI satellite observations and global model si, Atmospheric Chemistry and Physics, 14, 7909-7927, 10.5194/acp-14-7909-2014, 2014.

Keller, C. A., Knowland, K. E., Duncan, B. N., Liu, J., Anderson, D. C., Das, S., Lucchesi, R. A., Lundgren, E. W., Nicely, J. M., Nielsen, E., Ott, L. E., Saunders, E., Strode, S. A., Wales, P. A., Jacob, D. J., and Pawson, S.: Description of the NASA GEOS Composition Forecast Modeling System GEOS-CF v1.0, Journal of Advances in Modeling Earth Systems, 13, 10.1029/2020ms002413, 2021.

Kim, J., Jeong, U., Ahn, M.-H., Kim, J. H., Park, R. J., Lee, H., Song, C. H., Choi, Y.-S., Lee, K.-H., Yoo, J.-M., Jeong, M.-J., Park, S. K., Lee, K.-M., Song, C.-K., Kim, S.-W., Kim, Y. J., Kim, S.-W., Kim, M., Go, S., Liu, X., Chance, K., Chan Miller, C., Al-Saadi, J., Veihelmann, B., Bhartia, P. K., Torres, O., Abad, G. G., Haffner, D. P., Ko, D. H., Lee, S. H., Woo, J.-H., Chong, H., Park, S. S., Nicks, D., Choi, W. J., Moon, K.-J., Cho, A., Yoon, J., Kim, S.-K., Hong, H., Lee, K., Lee, H., Lee, S., Choi, M., Veefkind, P., Levelt, P. F., Edwards, D. P., Kang, M., Eo, M., Bak, J., Baek, K., Kwon, H.-A., Yang, J., Park, J.,

Han, K. M., Kim, B.-R., Shin, H.-W., Choi, H., Lee, E., Chong, J., Cha, Y., Koo, J.-H., Irie, H., Hayashida, S., Kasai, Y., Kanaya, Y., Liu, C., Lin, J., Crawford, J. H., Carmichael, G. R., Newchurch, M. J., Lefer, B. L., Herman, J. R., Swap, R. J., Lau, A. K. H., Kurosu, T. P., Jaross, G., Ahlers, B., Dobber, M., Mcelroy, C. T., and Choi, Y.: New Era of Air Quality Monitoring from Space: Geostationary Environment Monitoring Spectrometer (GEMS), Bulletin of the American Meteorological Society, 101, E1-E22, 10.1175/bams-d-18-0013.1, 2020.

Kim, S., Kim, D., Hong, H., Chang, L. S., Lee, H., Kim, D. R., Kim, D., Yu, J. A., Lee, D., Jeong, U., Song, C. K., Kim, S. W., Park, S. S., Kim, J., Hanisco, T. F., Park, J., Choi, W., and Lee, K.: First-time comparison between NO2 vertical columns from GEMS and Pandora measurements, Atmos. Meas. Tech. Discuss., 2023, 1-22, 10.5194/amt-2023-11, 2023.

Knowland, K. E., Keller, C. A., and Lucchesi, R. A.: File Specification for GEOS-CF Products, 2022a.

Knowland, K. E., Keller, C. A., Wales, P. A., Wargan, K., Coy, L., Johnson, M. S., Liu, J., Lucchesi, R. A., Eastham, S. D., Fleming, E., Liang, Q., Leblanc, T., Livesey, N. J., Walker, K. A., Ott, L. E., and Pawson, S.: NASA GEOS Composition Forecast Modeling System GEOS-CF v1.0: Stratospheric Composition, Journal of Advances in Modeling Earth Systems, 14, e2021MS002852, https://doi.org/10.1029/2021MS002852, 2022b.

Kong, H., Lin, J., Chen, L., Zhang, Y., Yan, Y., Liu, M., Ni, R., Liu, Z., and Weng, H.: Considerable Unaccounted Local Sources of NOx Emissions in China Revealed from Satellite, Environmental Science & Technology, 56, 7131-7142, 10.1021/acs.est.1c07723, 2022a.

Kong, H., Lin, J., Zhang, Y., Li, C., Xu, C., Shen, L., Liu, X., Yang, K., Su, H., and Xu, W.: Unexpected high NOX emissions from lakes on Tibetan Plateau under rapid warming, 10.21203/rs.3.rs-1980236/v1, 2022b.

Kong, H., Lin, J., Zhang, Y., Li, C., Xu, C., Shen, L., Liu, X., Yang, K., Su, H., and Xu, W.: High natural nitric oxide emissions from lakes on Tibetan Plateau under rapid warming, Nature Geoscience, 16, 474-477, 10.1038/s41561-023-01200-8, 2023.

Krotkov, N., Lamsal, L. N., Marchenko, S., and Swartz, W. H.: OMNO2 README Document Data Product Version 4.0, 2019.

Krotkov, N. A., McLinden, C. A., Li, C., Lamsal, L. N., Celarier, E. A., Marchenko, S. V., Swartz,

W. H., Bucsela, E. J., Joiner, J., Duncan, B. N., Boersma, K. F., Veefkind, J. P., Levelt, P. F., Fioletov, V. E., Dickerson, R. R., He, H., Lu, Z., and Streets, D. G.: Aura OMI observations of regional SO2 and NO2 pollution changes from 2005 to 2015, Atmos. Chem. Phys., 16, 4605-4629, 10.5194/acp-16-4605-2016, 2016.

Lee, H., Park, J., and Hong, H.: Geostationary Environment Monitoring Spectrometer (GEMS) Algorithm Theoretical Basis Document NO2 Retrieval Algorithm, 2020.

Lee, Y., Ahn, M. H., Kang, M., and Eo, M.: Spectral replacement using machine learning methods for continuous mapping of the Geostationary Environment Monitoring Spectrometer (GEMS), Atmos. Meas. Tech., 16, 153-168, 10.5194/amt-16-153-2023, 2023.

Levelt, P. F., Van Den Oord, G. H. J., Dobber, M. R., Malkki, A., Visser, H., Vries, J. D., Stammes, P., Lundell, J. O. V., and Saari, H.: The ozone monitoring instrument, IEEE Transactions on Geoscience and Remote Sensing, 44, 1093-1101, 10.1109/tgrs.2006.872333, 2006.

Li, J., Wang, Y., Zhang, R., Smeltzer, C., Weinheimer, A., Herman, J., Boersma, K. F., Celarier, E. A., Long, R. W., Szykman, J. J., Delgado, R., Thompson, A. M., Knepp, T. N., Lamsal, L. N., Janz, S. J., Kowalewski, M. G., Liu, X., and Nowlan, C. R.: Comprehensive evaluations of diurnal NO2 measurements during DISCOVER-AQ 2011: effects of resolution-dependent representation of NOx emissions, Atmos. Chem. Phys., 21, 11133-11160, 10.5194/acp-21-11133-2021, 2021a.

Li, K.-F., Khoury, R., Pongetti, T. J., Sander, S. P., Mills, F. P., and Yung, Y. L.: Diurnal variability of stratospheric column NO_2 measured using direct solar and lunar spectra over Table Mountain, California (34.38° N), Atmospheric Measurement Techniques, 14, 7495-7510, 10.5194/amt-14-7495-2021, 2021b.

Lin, J. T. and McElroy, M. B.: Detection from space of a reduction in anthropogenic emissions of nitrogen oxides during the Chinese economic downturn, Atmos. Chem. Phys., 11, 8171-8188, 10.5194/acp-11-8171-2011, 2011.

Lin, J. T., Liu, M. Y., Xin, J. Y., Boersma, K. F., Spurr, R., Martin, R., and Zhang, Q.: Influence of aerosols and surface reflectance on satellite NO2 retrieval: seasonal and spatial characteristics and implications for NOx emission constraints, Atmospheric Chemistry and Physics, 15, 11217-11241, 10.5194/acp-15-11217-2015, 2015.

Lin, J. T., Martin, R. V., Boersma, K. F., Sneep, M., Stammes, P., Spurr, R., Wang, P., Van

Roozendael, M., Clémer, K., and Irie, H.: Retrieving tropospheric nitrogen dioxide from the Ozone Monitoring Instrument: effects of aerosols, surface reflectance anisotropy, and vertical profile of nitrogen dioxide, Atmospheric Chemistry and Physics, 14, 1441-1461, 10.5194/acp-14-1441-2014, 2014.

Liu, M., Lin, J., Wang, Y., Sun, Y., Zheng, B., Shao, J., Chen, L., Zheng, Y., Chen, J., Fu, T. M., Yan, Y., Zhang, Q., and Wu, Z.: Spatiotemporal variability of NO2 and PM2.5 over Eastern China: observational and model analyses with a novel statistical method, Atmos. Chem. Phys., 18, 12933-12952, 10.5194/acp-18-12933-2018, ~~2018~~2018a.

Liu, M., Lin, J., Kong, H., Boersma, K. F., Eskes, H., Kanaya, Y., He, Q., Tian, X., Qin, K., Xie, P., Spurr, R., Ni, R., Yan, Y., Weng, H., and Wang, J.: A new TROPOMI product for tropospheric NO2 columns over East Asia with explicit aerosol corrections, Atmos. Meas. Tech., 13, 4247-4259, 10.5194/amt-13-4247-2020, 2020.

Liu, M., Lin, J., Boersma, K. F., Pinardi, G., Wang, Y., Chimot, J., Wagner, T., Xie, P., Eskes, H., Van Roozendael, M., Hendrick, F., Wang, P., Wang, T., Yan, Y., Chen, L., and Ni, R.: Improved aerosol correction for OMI tropospheric NO2 retrieval over East Asia: constraint from CALIOP aerosol vertical profile, Atmospheric Measurement Techniques, 12, 1-21, 10.5194/amt-12-1-2019, 2019.

Liu, Y.-H., Ma, J.-L., Li, L., Lin, X.-F., Xu, W.-J., and Ding, H.: A high temporal-spatial vehicle emission inventory based on detailed hourly traffic data in a medium-sized city of China, Environmental Pollution, 236, 324-333, https://doi.org/10.1016/j.envpol.2018.01.068, 2018b.

Lorente, A., Boersma, K. F., Stammes, P., Tilstra, L. G., and Muller, J. P.: The importance of surface reflectance anisotropy for cloud and NO2 retrievals from GOME-2 and OMI, 2018.

Lorente, A., Boersma, K. F., Yu, H., Dorner, S., Hilboll, A., Richter, A., Liu, M., Lamsal, L. N., Barkley, M. P., and De Smedt, I.: Structural uncertainty in air mass factor calculation for NO2 and HCHO satellite retrievals, Atmospheric Measurement Techniques, 10, 759-782, 2016.

Lucht, W., Schaaf, C. B., and Strahler, A. H.: An algorithm for the retrieval of albedo from space using semiempirical BRDF models, IEEE Transactions on Geoscience & Remote Sensing, 38, 977-998, 2000.

~~Richter, A., Begoin, M., Hilboll, A., and Burrows, J. P.: An improved NO2 retrieval for the GOME-2 satellite instrument, Atmospheric Measurement Techniques, 4, 1147-1159, 10.5194/amt-4-1147-2011, 2011.~~

Naiudomthum, S., Winijkul, E., and Sirisubtawee, S.: Near Real-Time Spatial and Temporal Distribution of Traffic Emissions in Bangkok Using Google Maps Application Program Interface, Atmosphere, 13, 1803, 10.3390/atmos13111803, 2022.

Palmer, P. I., Jacob, D. J., Chance, K., Martin, R. V., Spurr, R. J. D., Kurosu, T. P., Bey, I., Yantosca, R., Fiore, A., and Li, Q.: Air mass factor formulation for spectroscopic measurements from satellites: Application to formaldehyde retrievals from the Global Ozone Monitoring Experiment, Journal of Geophysical Research: Atmospheres, 106, 14539-14550, 10.1029/2000jd900772, 2001.

Richter, A., Burrows, J. P., Nüß, H., Granier, C., and Niemeier, U.: Increase in tropospheric nitrogen dioxide over China observed from space, Nature, 437, 129-132, 10.1038/nature04092, 2005.

Shindell, D. T., Faluvegi, G., Koch, D. M., Schmidt, G. A., Unger, N., and Bauer, S. E.: Improved Attribution of Climate Forcing to Emissions, Science, 326, 716-718, 10.1126/science.1174760, 2009.

Valks, P.: Algorithm Theoretical Basis Document for GOME-2 Total Column Products of Ozone, NO2, BrO, SO2, H2O, HCHO, OClO and Cloud Properties (GDP 4.8/4.9), 2019.

Valks, P., Chan, L., Zimmer, W., Hedelt, P., and Slijkhuis, S.: PRODUCT USER MANUAL GOME-2 Total Column Products of Ozone, NO2, BrO, HCHO, SO2, H2O, OClO and Cloud Properties GDP 4.8 for GOME-2 on MetOp-A and -B GDP 4.9 for GOME-2 on MetOp-C, 2019.

van der A, R. J., Mijling, B., Ding, J., Koukouli, M. E., Liu, F., Li, Q., Mao, H., and Theys, N.: Cleaning up the air: effectiveness of air quality policy for SO2 and NOx emissions in China, Atmos. Chem. Phys., 17, 1775-1789, 10.5194/acp-17-1775-2017, 2017.

Van Geffen, J., Eskes, H., Boersma, K. F., and Veefkind, P.: TROPOMI ATBD of the total and tropospheric NO2 data products, 2022a.

Van Geffen, J., Boersma, K. F., Eskes, H., Sneep, M., Ter Linden, M., Zara, M., and Veefkind, J. P.: S5P TROPOMI NO$_2$ slant column retrieval: method, stability, uncertainties and comparisons with OMI, Atmospheric Measurement Techniques, 13, 1315-1335, 10.5194/amt-13-1315-2020, 2020.

Van Geffen, J., Eskes, H., Compernolle, S., Pinardi, G., Verhoelst, T., Lambert, J.-C., Sneep, M., Ter Linden, M., Ludewig, A., Boersma, K. F., and Veefkind, J. P.: Sentinel-5P TROPOMI NO$_2$ retrieval: impact of version v2.2 improvements and comparisons with OMI and ground-based data, Atmospheric Measurement Techniques, 15, 2037-2060, 10.5194/amt-15-2037-2022,

2022b.

van Geffen, J. H. G. M., Boersma, K. F., Van Roozendael, M., Hendrick, F., Mahieu, E., De Smedt, I., Sneep, M., and Veefkind, J. P.: Improved spectral fitting of nitrogen dioxide from OMI in the 405-465 nm window, Atmos. Meas. Tech., 8, 1685-1699, 10.5194/amt-8-1685-2015, 2015.

Vasilkov, A., Krotkov, N., Yang, E. S., Lamsal, L., Joiner, J., Castellanos, P., Fasnacht, Z., and Spurr, R.: Explicit and consistent aerosol correction for visible wavelength satellite cloud and nitrogen dioxide retrievals based on optical properties from a global aerosol analysis, Atmos. Meas. Tech., 14, 2857-2871, 10.5194/amt-14-2857-2021, 2021.

Vasilkov, A. P., Qin, W., Krotkov, N. A., Lamsal, L. N., Spurr, R., Haffner, D. P., Joiner, J., Yang, E., and Marchenko, S.: Accounting for the Effects of Surface BRDF on Satellite Cloud and Trace-Gas Retrievals: A New Approach Based on Geometry-Dependent Lambertian-Equivalent Reflectivity Applied to OMI Algorithms, Atmospheric Measurement Techniques, 10, 333-349, 2016.

Veefkind, J. P., Aben, I., McMullan, K., Förster, H., de Vries, J., Otter, G., Claas, J., Eskes, H. J., de Haan, J. F., Kleipool, Q., van Weele, M., Hasekamp, O., Hoogeveen, R., Landgraf, J., Snel, R., Tol, P., Ingmann, P., Voors, R., Kruizinga, B., Vink, R., Visser, H., and Levelt, P. F.: TROPOMI on the ESA Sentinel-5 Precursor: A GMES mission for global observations of the atmospheric composition for climate, air quality and ozone layer applications, Remote Sensing of Environment, 120, 70-83, https://doi.org/10.1016/j.rse.2011.09.027, 2012.

Wei, J., Liu, S., Li, Z., Liu, C., Qin, K., Liu, X., Pinker, R. T., Dickerson, R. R., Lin, J., Boersma, K. F., Sun, L., Li, R., Xue, W., Cui, Y., Zhang, C., and Wang, J.: Ground-Level NO_2 Surveillance from Space Across China for High Resolution Using Interpretable Spatiotemporally Weighted Artificial Intelligence, Environmental Science & Technology, 56, 9988-9998, 10.1021/acs.est.2c03834, 2022.

Weng, H., Lin, J., Martin, R., Millet, D. B., Jaeglé, L., Ridley, D., Keller, C., Li, C., Du, M., and Meng, J.: Global high-resolution emissions of soil NOx, sea salt aerosols, and biogenic volatile organic compounds, Scientific Data, 7, 148, 10.1038/s41597-020-0488-5, 2020.

Yang, L. H., Jacob, D. J., Colombi, N. K., Zhai, S., Bates, K. H., Shah, V., Beaudry, E., Yantosca, R. M., Lin, H., Brewer, J. F., Chong, H., Travis, K. R., Crawford, J. H., Lamsal, L. N., Koo, J. H., and Kim, J.: Tropospheric NO2 vertical profiles over South Korea and their relation to oxidant chemistry:

implications for geostationary satellite retrievals and the observation of NO2 diurnal variation from space, Atmos. Chem. Phys., 23, 2465-2481, 10.5194/acp-23-2465-2023, 2023.

Zhang, Y., Lin, J., Liu, M., Kong, H., Chen, L., Weng, H., and Li, C.: High-resolution Tropospheric NO2 Retrieval over Asia based on OMI POMINO v2.1 and Quantitative comparison with other products, National Remote Sensing Bulletin, 10.11834/jrs.20221413, 2022.

Zhou, Y., Brunner, D., Spurr, R. J. D., Boersma, K. F., Sneep, M., Popp, C., and Buchmann, B.: Accounting for surface reflectance anisotropy in satellite retrievals of tropospheric NO2, Atmospheric Measurement Techniques, 3, 1185-1203, 2010.